

Geometric Exponents, SLE and Logarithmic Minimal Models

Yvan Saint-Aubin*

*Département de mathématiques et de statistique
Université de Montréal, C.P. 6128, succ. centre-ville, Montréal
Québec, Canada, H3C 3J7*

Paul A. Pearce[†] Jørgen Rasmussen[‡]

*Department of Mathematics and Statistics
University of Melbourne
Parkville, Victoria 3010, Australia*

Abstract

In statistical mechanics, observables are usually related to local degrees of freedom such as the $Q < 4$ distinct states of the Q -state Potts models or the heights of the restricted solid-on-solid models. In the continuum scaling limit, these models are described by rational conformal field theories, namely the minimal models $\mathcal{M}(p, p')$ for suitable p, p' . More generally, as in stochastic Loewner evolution (SLE_κ), one can consider observables related to nonlocal degrees of freedom such as paths or boundaries of clusters. This leads to fractal dimensions or geometric exponents related to values of conformal dimensions not found among the finite sets of values allowed by the rational minimal models. Working in the context of a loop gas with loop fugacity $\beta = -2 \cos \frac{4\pi}{\kappa}$, we use Monte Carlo simulations to measure the fractal dimensions of various geometric objects such as paths and the generalizations of cluster mass, cluster hull, external perimeter and red bonds. Specializing to the case where the SLE parameter $\kappa = \frac{4p'}{p}$ is rational with $p < p'$, we argue that the geometric exponents are related to conformal dimensions found in the infinitely extended Kac tables of the logarithmic minimal models $\mathcal{LM}(p, p')$. These theories describe lattice systems with nonlocal degrees of freedom. We present results for critical dense polymers $\mathcal{LM}(1, 2)$, critical percolation $\mathcal{LM}(2, 3)$, the logarithmic Ising model $\mathcal{LM}(3, 4)$, the logarithmic tricritical Ising model $\mathcal{LM}(4, 5)$ as well as $\mathcal{LM}(3, 5)$. Our results are compared with rigorous results from SLE_κ , with predictions from theoretical physics and with other numerical experiments. Throughout, we emphasize the relationships between SLE_κ , geometric exponents and the conformal dimensions of the underlying CFTs.

Keywords: SLE, CFT, fractal dimensions, geometric exponents, logarithmic minimal models.

*saint@dms.umontreal.ca

[†]P.Pearce@ms.unimelb.edu.au

[‡]J.Rasmussen@ms.unimelb.edu.au

Contents

1	Introduction	2
2	SLE and CFT	4
2.1	SLE	4
2.2	Logarithmic minimal models and CFT	5
2.3	Relation between geometric exponents and conformal dimensions	5
3	Fractal dimension of a defect	6
3.1	Definition and measurements	6
3.2	Technical issues	10
3.2.1	Probability distribution of $d_D^{H \times V}$ and error on measurements	10
3.2.2	Extracting \widehat{d}_D from $\{d_{D,1}^{H \times V}\}$ and $\{d_{D,2}^{H \times V}\}$	12
3.2.3	Importance of boundary half-circles	15
4	Other geometric objects: hull, cluster mass, external perimeter and red bonds	16
4.1	Definition of masses for loop gas clusters	16
4.2	Measurements	21
4.3	Technical issues	23
4.3.1	Estimates of critical percolation masses from smaller data windows	23
4.3.2	The definitions of the loop external perimeter	23
4.3.3	d_H and d_{EP} for configurations with one and two defects	26
A	Loop gas and logarithmic minimal models	27
B	Upgrade algorithms	29
B.1	Critical percolation ($\beta = 1$)	29
B.2	Models with $0 < \beta \leq 2$	29
B.3	Critical dense polymers ($\beta = 0$)	31
C	Initial thermalization and independence of measurements	31

1 Introduction

The numerical measurements of fractal dimensions and geometric exponents presented here aim at strengthening the ties between three central paradigms describing two-dimensional phase transitions. The first, the lattice approach, which started with Onsager’s calculation [1] of the spectrum of the transfer matrix of the Ising model and continued in the work of Baxter [2], is the closest to a first-principle description of phase transitions. Rigorous results obtained from this approach are important, but remain far from the more physical continuum field-theoretic description used in solid-state or elementary particle physics. By limiting the description to the critical point, the second paradigm, conformal field theory (CFT) [3], has provided such a full-fledged continuum field theory with exact calculations of certain correlation functions. In doing so, it enlarges the set of algebraic tools, already central in Onsager’s solution, that describe critical behaviour. Even though CFT enables perturbation away from criticality, the approach to criticality is far from being understood. Moreover, its description of statistical models misses the probability framework that one would expect from models whose ab initio description uses the Boltzmann distribution. The third paradigm, Stochastic Loewner Evolution (SLE) [4, 5, 6, 7, 8, 9, 10], is indeed probabilistic in nature. In SLE, objects are of a measure-theoretic nature and are concrete enough to reproduce rigorously several predictions from the other two approaches, mostly those from CFT. Since rigorous derivations [11] give the fractal dimension of certain SLE paths confirming predictions from CFT, it seems natural to us that the study of fractal properties of critical geometric objects will improve the understanding of the ties between the three paradigms of lattice statistics, CFT and SLE.

Many geometric objects have been introduced to probe the critical behaviour of lattice models: the hull of a spin cluster, its mass, its external perimeter and its red bonds. In contrast to the usual correlation functions of local degrees of freedom, these geometric observables relate to nonlocal objects on the lattice. Theoretical predictions for various fractal dimensions and geometric scaling exponents were made in the late eighties [12]. Many numerical measurements have been made, but only relatively recently were good measurements [13, 14, 15] made of the fractal dimensions of these objects. These support the theoretical predictions but are limited to the Fortuin-Kasteleyn (FK) clusters [16] of Q -state Potts models [17].

The basic random variables in lattice spin models used for Monte Carlo (MC) simulations are the Potts spins sitting at the vertices of the lattice. Reasons to use Potts spin models for these simulations are numerous. First, spin variables are close to physical objects, readily interpretable as originating from an atom in a crystal. Second, the Swendsen-Wang algorithm [18] provides extremely quick upgrades in MC simulations. Third, the thermodynamic limits of three of the Q -Potts models are archetypal lattice statistical models, namely, critical percolation ($Q \rightarrow 1$) with central charge $c = 0$, the Ising model ($Q = 2$) with $c = \frac{1}{2}$ and the 3-state Potts model with $c = \frac{4}{5}$.

The continuum scaling limits of the $Q = 2, 3$ Potts models are described by rational CFTs. More explicitly, they are described by the members $\mathcal{M}(3, 4)$ and $\mathcal{M}(5, 6)$ of the series of minimal models $\mathcal{M}(p, p')$ [19, 20] with central charges

$$c = c(\bar{\kappa}) = 1 - \frac{6(1 - \bar{\kappa})^2}{\bar{\kappa}} = 13 - 6\left(\bar{\kappa} + \frac{1}{\bar{\kappa}}\right), \quad \bar{\kappa} = \frac{p'}{p} > 1, \quad p, p' > 1 \text{ coprime} \quad (1.1)$$

related to Q by the mapping

$$\sqrt{Q} = -2 \cos \frac{\pi}{\bar{\kappa}}, \quad Q < 4. \quad (1.2)$$

But now we are immediately presented with two problems. First, critical percolation, which formally is an allowed minimal model corresponding to $p = 2, p' = 3$, is *empty* in the sense that it only contains the identity with conformal dimension $\Delta = 0$. Second and more generally, the conformal dimensions related to the nonlocal geometric observables are not found [12] among the admissible conformal dimensions in the Kac tables for these rational CFTs.

To circumvent these problems in considering fractal geometric objects, we follow [21, 22] and move the lattice context away from the rational Q -state Potts or Restricted Solid-On-Solid (RSOS) models [20] and instead consider a loop gas with loop fugacity

$$\beta = -2 \cos \frac{\pi}{\bar{\kappa}}. \quad (1.3)$$

We believe there is good ground to measure the fractal dimensions of suitable geometric objects directly in the loop gas. In the loop gas, the basic random variables are the nonlocal degrees of freedom associated with segments of the loops. The continuum scaling limit of such a loop gas is not described by a rational CFT — it is described by the Coulomb gas [23, 3]. Moreover, if $\bar{\kappa}$ is rational, which is the case of prime interest here, the loop gas is equivalent to the logarithmic minimal model $\mathcal{LM}(p, p')$ [24] and exhibits some remarkable properties. In the continuum scaling limit, it is thus described by a *logarithmic* CFT [25] with central charge given by the same expression as in the rational case (1.1)

$$c = 1 - \frac{6(1 - \bar{\kappa})^2}{\bar{\kappa}} = 13 - 6\left(\bar{\kappa} + \frac{1}{\bar{\kappa}}\right), \quad \bar{\kappa} = \frac{p'}{p} > 1, \quad p, p' \geq 1 \text{ coprime}. \quad (1.4)$$

It is noted, though, that the logarithmic minimal model $\mathcal{LM}(p, p')$ is defined also for $p = 1$. Critical dense polymers, with $c = -2$, now appears as the member $\mathcal{LM}(1, 2)$ and critical percolation as the member $\mathcal{LM}(2, 3)$. For recent studies of critical percolation as a logarithmic CFT, we refer to [26] and references therein. As we will argue in many cases, the conformal dimensions related to the observed geometric exponents are found among the conformal dimensions in the *infinitely* extended Kac tables (2.3) for these logarithmic CFTs.

The basic probabilistic object of chordal SLE_{κ} is a path or curve with (at least) its starting point on the boundary of the domain within which it evolves. The evolution is described by (2.1) where we identify

$$\kappa = 4\bar{\kappa}. \quad (1.5)$$

Probabilists working with SLE use $\kappa = 6$ for critical percolation while physicists working with CFT use $\bar{\kappa} = \frac{3}{2}$. One can argue that studying a lattice loop gas is to probe directly a discretized version of SLE paths. Alternatively, it has been proved for some values of κ that the curves formed by loop segments of the loop gas coincide, in the continuum scaling limit, with SLE paths. Throughout this paper, we will emphasize the relationships between SLE, geometric exponents and the conformal dimensions of the underlying CFTs. As already indicated, for rational values of $\bar{\kappa} = p'/p$, we argue that the relevant underlying CFT is that of the logarithmic minimal model $\mathcal{LM}(p, p')$.

The paper is organized as follows. The next section recalls the definition of the SLE process and summarizes the theoretical predictions for the fractal dimensions and geometric exponents of interest. Section 3 is devoted to the measurement of the fractal dimension of a path associated with a defect. This is the most natural discretization of an SLE path. Section 4 introduces natural extensions of classical geometric objects (cluster hull, cluster mass, external perimeter and red bonds) to the context of a loop gas. The measurement of these quantities by MC methods is also presented in this section. The lattice loop gas and the logarithmic minimal models $\mathcal{LM}(p, p')$ are recalled in Appendix A. The various MC upgrade algorithms that we use are discussed in Appendix B. Finally, in Appendix C, we describe the initial thermalization of the MC process as well as checks on the statistical independence of our measurements.

2 SLE and CFT

2.1 SLE

Two landmark results led to the development of SLE as a tool to probe critical phenomena. One of them is Smirnov's proof [27] that one observable of critical percolation on the triangular lattice has a scaling limit that is conformally invariant. The second is the introduction by Schramm [4] of a one-parameter family of conformally invariant measures on curves in the half-plane, denoted by SLE_κ . Schramm also showed that this family exhausts all such conformally invariant measures. Hence, the measure on interfaces of percolating clusters must fall in this family. Schramm showed that SLE_6 was the one.

A simple way to understand this measure is to see the interfaces (or curves) as being grown out of a point on the real line, the boundary of the half-plane. During the growth, the interface may touch itself or the real line. Points belonging to the interface and points from which a curve cannot be drawn to infinity without crossing the interface form the SLE hull.

Let us denote by \mathcal{C}_t the complement of the hull at time t . Then $\mathcal{C}_t \cap \mathbb{H}$ is a simply-connected open set and, by the Riemann mapping theorem, there exists an analytic function $g_t : \mathcal{C}_t \cap \mathbb{H} \rightarrow \mathbb{H}$ that is one-to-one. It is this map g_t that satisfies the stochastic Loewner equation:

$$\partial_t g_t(z) = \frac{2}{g_t(z) - \sqrt{\kappa} B_t}, \quad t > 0, \quad \text{with } g_0(z) = z, \quad (2.1)$$

where B_t is a one-dimensional Brownian motion starting at 0. To determine uniquely g_t , its behaviour around infinity is fixed by $\lim_{z \rightarrow \infty} (g_t(z) - z) = 0$. The interface $\gamma = \gamma_t$ is then defined as the (continuous) path $\gamma : [0, \infty) \rightarrow \mathbb{H}$ with $g_t(\gamma_t) = \sqrt{\kappa} B_t$. Equation (2.1) determines (somewhat implicitly) the probabilistic properties of γ_t in terms of those of the Brownian motion.

One of the important corollaries of stochastic Loewner evolution is that the curve γ generated by the process with parameter κ has Hausdorff dimension equal to

$$d_{\text{path}}^{\text{SLE}} = \min(2, 1 + \frac{\kappa}{8}) \quad (2.2)$$

almost surely. This result, due to Beffara [11], together with the fact that the scaling limit of percolation is SLE_6 , proves one of the important predictions of theoretical physics, at least for one model on a very particular lattice. If one believes in universality, then the result should also apply to other lattices. Note that, if one sets $\kappa = 0$ in (2.1), the measure degenerates and the interface γ_t tracing the imaginary axis has probability one. The fractal dimension of γ is then 1. For κ larger or equal to 8, the curve is space filling and has dimension 2.

2.2 Logarithmic minimal models and CFT

The logarithmic minimal models $\mathcal{LM}(p, p')$ [24] are reviewed briefly in Appendix A. The degrees of freedom of these theories are nonlocal objects associated with segments of the loops. In the continuum scaling limit, these models are described by logarithmic CFTs with central charges (1.4). Conformal dimensions of these CFTs can be organized into infinitely extended Kac tables

$$\Delta_{r,s} = \frac{(\bar{\kappa}r - s)^2 - (\bar{\kappa} - 1)^2}{4\bar{\kappa}}, \quad r, s \in \mathbb{N}. \quad (2.3)$$

There is no claim here, however, that these values exhaust all possible values of the conformal dimensions for these theories. Indeed, there is some evidence [12] that conformal dimensions corresponding to half-integer values of r and s are allowed.

There is a duality in these theories, mimicked in SLE_κ and described by

$$p \leftrightarrow p', \quad \text{or} \quad \kappa \leftrightarrow \frac{16}{\kappa}, \quad \text{or} \quad \bar{\kappa} \leftrightarrow \frac{1}{\bar{\kappa}}. \quad (2.4)$$

Under this duality, the central charges and conformal dimensions verify

$$c(\bar{\kappa}) = c\left(\frac{1}{\bar{\kappa}}\right), \quad \Delta_{r,s}\left(\frac{1}{\bar{\kappa}}\right) = \Delta_{s,r}(\bar{\kappa}). \quad (2.5)$$

Here we only consider the case $p < p'$ with $\bar{\kappa} = \frac{p'}{p} > 1$. From the lattice, the dual models with $p > p'$ and $\bar{\kappa} < 1$ are expected to come from the dilute logarithmic minimal models with central charge $c(\bar{\kappa}) = c\left(\frac{1}{\bar{\kappa}}\right)$ but we do not consider these models here.

2.3 Relation between geometric exponents and conformal dimensions

An important challenge is to relate the values of various geometric exponents or fractal dimensions d of observables to the conformal dimensions Δ of correlators

$$\langle \phi(0)\phi(x) \rangle \sim |x|^{-2\Delta} \quad (2.6)$$

in the underlying CFTs, for example the critical Q -state Potts models. For Q integer, these are rational CFTs with relatively few conformal dimensions and sometimes one is led to conformal dimensions not found among the admissible values for these rational theories. Some observables in the logarithmic minimal models $\mathcal{LM}(p, p')$ should correspond to observables in the Potts models related to FK clusters. In addition, however, the logarithmic minimal models $\mathcal{LM}(p, p')$ allow us to explain many observables *not* explained by the rational models. Consider a geometric observable \mathcal{O} , measured on FK clusters of linear scale or radius R and described by correlators of the field ϕ . An example is C , the cluster mass (total number of sites) of a percolating cluster, or H , its hull. A heuristic scaling argument in two dimensions then gives

$$\mathcal{O}(R) \sim \int d^2x \langle \phi(0)\phi(x) \rangle \sim \int d^2x |x|^{-2\Delta} \sim R^{2-2\Delta} \sim R^{d_{\mathcal{O}}} \quad (2.7)$$

where $d_{\mathcal{O}}$ stands for the fractal dimension of the observable \mathcal{O} . In this way, such observables are associated with particular conformal weights in the Kac table. The renormalization group or geometric exponent y is related to Δ by

$$y = 2 - 2\Delta = d_{\mathcal{O}}. \quad (2.8)$$

In Section 3, we verify, through MC simulations, that precisely the fractal dimensions given in (2.2) are found in the continuum scaling limit of the logarithmic minimal models $\mathcal{LM}(p, p')$ with boundary conditions imposing a single (chordal) defect propagating through the system. We find it natural to identify this defect with (a discretized version of) the SLE path. We also note that for all p, p' , the dimension $d_{\text{path}}^{\text{SLE}}$ given above corresponds to

$$d_{\text{path}}^{\text{SLE}} = 2 - 2\Delta_{p,p'-1} = y_{p,p'-1} \quad (2.9)$$

where $\Delta_{p,p'-1}$ is a conformal dimension (2.3) of the logarithmic minimal model that falls outside the rational Kac table.

In Section 4.1, we recall the definitions of the hull, cluster mass, external perimeter and red bonds for the context of the FK clusters of the Q-state Potts models and show how these definitions can be extended to logarithmic minimal models $\mathcal{LM}(p, p')$. The fractal dimensions (cluster mass) of FK clusters are given by (see [10, 15] and references therein)

$$\Delta_C^{\text{FK}} = \Delta_\sigma = \frac{1}{2} - \frac{3\bar{\kappa}}{16} - \frac{1}{4\bar{\kappa}}, \quad d_C^{\text{FK}} = 1 + \frac{3\bar{\kappa}}{8} + \frac{1}{2\bar{\kappa}} \quad (2.10)$$

with the identification

$$C = \{\text{Cluster mass}\} \leftrightarrow \Delta_\sigma = \Delta_{(p \pm 1)/2, p'/2}. \quad (2.11)$$

Notice that, depending on the parities of p and p' , the Kac labels here can take half-integer values as foreshadowed after (2.3). We also have the following associations (see [10, 28] and references therein)

$$H = \{\text{Hull}\} \leftrightarrow \Delta_{p, p' \pm 1}, \quad EP = \{\text{External Perimeter}\} \leftrightarrow \Delta_{p \pm 1, p'}, \quad RB = \{\text{Red Bonds}\} \leftrightarrow \Delta_{p, p' \pm 2} \quad (2.12)$$

with conformal and fractal dimensions

$$\Delta_H^{\text{FK}} = \Delta_{p, p' \pm 1} = \frac{1}{2} - \frac{\bar{\kappa}}{4}, \quad d_H^{\text{FK}} = 1 + \frac{\bar{\kappa}}{2} \quad (2.13)$$

$$\Delta_{EP}^{\text{FK}} = \Delta_{p \pm 1, p'} = \frac{1}{2} - \frac{1}{4\bar{\kappa}}, \quad d_{EP}^{\text{FK}} = 1 + \frac{1}{2\bar{\kappa}} \quad (2.14)$$

$$\Delta_{RB}^{\text{FK}} = \Delta_{p, p' \pm 2} = \frac{1}{2} - \frac{\bar{\kappa}}{4} + \frac{3}{4\bar{\kappa}}, \quad d_{RB}^{\text{FK}} = 1 + \frac{\bar{\kappa}}{2} - \frac{3}{2\bar{\kappa}} \quad (2.15)$$

We summarize in Table 1 the values of the fractal dimensions of these observables for the logarithmic minimal models $\mathcal{LM}(p, p')$ that will be studied. In Section 4, we verify, through MC simulations, that precisely these fractal dimensions are found by looking at suitably defined nonlocal observables of these logarithmic minimal models $\mathcal{LM}(p, p')$. We note that the fractal dimension of the cluster hull d_H coincides with the fractal dimension of the SLE path $d_{\text{path}}^{\text{SLE}}$.

3 Fractal dimension of a defect

3.1 Definition and measurements

For the simulations, we use the logarithmic minimal model $\mathcal{LM}(p, p')$, a loop gas introduced in [24]. Some very rudimentary properties of these models are recalled in Appendix A. When the parameter $\bar{\kappa}$ characterizing the model is chosen to describe one of the Q-Potts models, the distribution of the loops coincides with that of the FK contours. We refer to an open curve in a loop configuration, that is, one starting and ending on the boundary of the domain considered, as a *defect*. Because of the parallel between loops in the logarithmic minimal models and interfaces of FK graphs, it is natural to consider a defect as a (discretized version of a) chordal SLE process. The goal of the present section is to measure the fractal dimension of such a defect for models corresponding to various values of $\bar{\kappa}$ of the SLE process. In the case of critical dense polymers $\mathcal{LM}(1, 2)$ where $\bar{\kappa} = 2$, the loop fugacity vanishes, $\beta = 0$, hence excluding all configurations with at least one closed loop. In this model, the defect fills the space and the agreement with $d_{\text{path}}^{\text{SLE}} = 2$ is trivial. This model is not studied further in this section.

There are various definitions of dimension for objects of fractal nature. The Hausdorff dimension is widely used in analysis, but it is customary to use the Minkowski definition for simulations. Let D be a set $D \subset \mathbb{R}^d$ and let $N(\epsilon)$ be the number of boxes of side length ϵ required to cover D in an evenly-spaced grid. The Minkowski dimension of D is then given by

$$d_D = \lim_{\epsilon \rightarrow 0} \frac{\log N(\epsilon)}{\log(1/\epsilon)} \quad (3.1)$$

if the limit exists. There are sets whose Hausdorff and Minkowski dimensions differ, but this subtlety is somewhat irrelevant here since we are to approximate the measurement of fractal objects by studying *finite* geometric objects.

model	κ	$\bar{\kappa}$	c	$\beta = \sqrt{Q}$	d_H	d_C	d_{EP}	d_{RB}
$\mathcal{LM}(p, p')$	$\frac{4p'}{p}$	$\frac{p'}{p}$	$13 - 6\bar{\kappa} - \frac{6}{\bar{\kappa}}$	$-2 \cos \frac{\pi}{\bar{\kappa}}$	$1 + \frac{\bar{\kappa}}{2}$	$1 + \frac{3\bar{\kappa}}{8} + \frac{1}{2\bar{\kappa}}$	$1 + \frac{1}{2\bar{\kappa}}$	$1 + \frac{\bar{\kappa}}{2} - \frac{3}{2\bar{\kappa}}$
$\mathcal{LM}(1, 2)$	8	2	-2	0	2	2	$\frac{5}{4}$	$\frac{5}{4}$
$\mathcal{LM}(3, 5)$	$\frac{20}{3}$	$\frac{5}{3}$	$-\frac{3}{5}$	$\frac{1}{2}(\sqrt{5} - 1)$	$\frac{11}{6}$	$\frac{77}{40}$	$\frac{13}{10}$	$\frac{14}{15}$
$\mathcal{LM}(2, 3)$	6	$\frac{3}{2}$	0	1	$\frac{7}{4}$	$\frac{91}{48}$	$\frac{4}{3}$	$\frac{3}{4}$
$\mathcal{LM}(3, 4)$	$\frac{16}{3}$	$\frac{4}{3}$	$\frac{1}{2}$	$\sqrt{2}$	$\frac{5}{3}$	$\frac{15}{8}$	$\frac{11}{8}$	$\frac{13}{24}$
$\mathcal{LM}(4, 5)$	5	$\frac{5}{4}$	$\frac{7}{10}$	$\frac{1}{2}(\sqrt{5} + 1)$	$\frac{13}{8}$	$\frac{299}{160}$	$\frac{7}{5}$	$\frac{17}{40}$

Table 1: The models, their parameters κ , $\bar{\kappa}$, c , β and fractal dimensions. The models include critical dense polymers $\mathcal{LM}(1, 2)$, critical percolation $\mathcal{LM}(2, 3)$, the logarithmic Ising model $\mathcal{LM}(3, 4)$ and the logarithmic tricritical Ising model $\mathcal{LM}(4, 5)$. The notations H, C, EP, RB stand for Hull, Cluster mass, External Perimeter and Red Bonds. The fractal dimension of the hull coincides with the fractal dimension of the SLE path $d_{\text{path}}^{\text{SLE}}$ as given in (2.2). The fractal dimensions of the cluster, external perimeter and red bonds coincide with those of the FK clusters in the associated Q-state Potts models via (1.2).

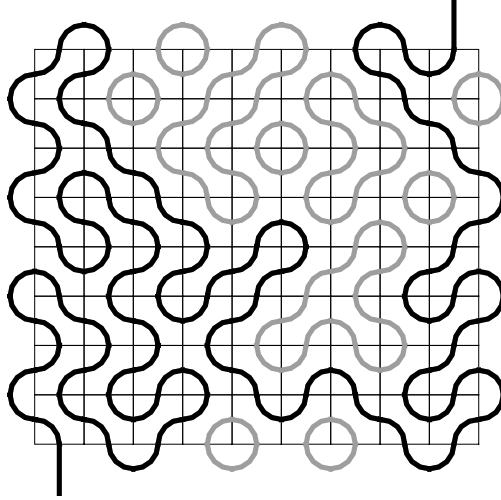


Figure 1: A configuration on a $H \times V = 9 \times 8$ lattice. The defect visits $N_\Delta = 104$ quarter-circles, including the ones on the boundary.

The objective here is to examine, using simulations, whether the fractal dimension of a defect d_D indeed corresponds to the fractal dimension of the SLE path $d_{\text{path}}^{\text{SLE}}$

$$d_D \stackrel{?}{=} d_{\text{path}}^{\text{SLE}}. \quad (3.2)$$

However, since we work on a finite lattice, say of size $H \times V$, we want to consider a discretization $d_D^{H \times V}$ of

the fractal dimension defined on the *finite* lattice yet approximating d_D in the infinite limit. One may think of the object D (the defect) as being drawn on a rectangle whose size and aspect ratio are fixed; the increase in H and V , while keeping their ratio fixed, then amounts to the limiting process. Therefore, if the size of the rectangle is fixed, $H \times V$ is related to the side length ϵ of a box as $H \times V \sim \frac{1}{\epsilon^2}$ or

$$\log(1/\epsilon) \sim \frac{1}{2} \log(\# \text{ of boxes}). \quad (3.3)$$

In fact, as each box can be crossed twice, one should instead count the number of quarter-circles, that is, the number of half-boxes. We therefore consider

$$d_D^{H \times V} \sim 2 \times \frac{\log N_\Delta(D)}{\log(2H \times V)} \sim \frac{\log N_\Delta(D)}{\log(R)} \quad (3.4)$$

where $N_\Delta(D)$ is the number of quarter-circles the defect D visits and where we have introduced some linear scale R . Up to a linear factor, R should be approximately $(2H \times V)^{\frac{1}{2}}$. If the defect crosses the same box twice, this counts for 2 in $N_\Delta(D)$. Figure 1 depicts the setting that we use for measurements of $d_D^{H \times V}$. The lattice is chosen to be almost square as the number H of boxes in a row is equal to $V + 1$ where V is the number of boxes in a column. We take V to be even. This allows for all loops on vertical boundaries to be closed by half-circles, as depicted in the figure. Because $H = V + 1$, all loops but one reaching a horizontal boundary can also be closed by half-circles. If we choose the pair of loose ends at the top right and bottom left, respectively, the *defect* will cross the lattice and be a macroscopic object. It is for this geometric object that N_Δ is computed for each configuration of the sample. To probe the asymptotic limit d_D , we will have to repeat these measurements on several lattices, starting with very small ones $H \times V = 3 \times 2$ and proceeding to 513×512 or 1025×1024 , depending on the model.

The technical details of the statistical analysis are given in Section 3.2. Here we present the results. We study four models: critical percolation $\mathcal{LM}(2, 3)$ and the logarithmic Ising model $\mathcal{LM}(3, 4)$ but also two which do not have Potts model cousins, namely the model $\mathcal{LM}(3, 5)$ with $c = -\frac{3}{5}$ and $\kappa = \frac{20}{3}$ and the logarithmic tricritical Ising model $\mathcal{LM}(4, 5)$ with $c = \frac{7}{10}$ and $\kappa = 5$. The results for the latter models demonstrate that fractal dimensions can be measured also for models not having Potts model cousins. For all four models, measurements are made of $d_D^{H \times V}$ for several lattice sizes in two different ways, as described in Section 3.2. The results are plotted in Figure 2. Fits are made for both sets, discarding the smallest lattices. The full curves go from the smallest to the largest lattices used for the fit. The fitted curves are extended with dashed lines to the rejected measurements. Numerical results appear in Table 2. The datum 1.835|1, for example, means that the 95%-confidence interval is of 1 unit of the last digit of 1.835. We stress that this is the interval due to statistical uncertainty of the measurements. The asymptotic behaviour is very good for the models $\mathcal{LM}(3, 5)$, $\mathcal{LM}(2, 3)$ and $\mathcal{LM}(3, 4)$. There is a slight departure from the predicted theoretical value in the case of the logarithmic tricritical Ising model $\mathcal{LM}(4, 5)$. One notices that the 95%-confidence interval does not always contain the theoretical prediction. The analysis in 3.2.2, however, will show how delicate the implied extrapolation is.

The setting for our simulations is quite different from those used in previous measurements [13, 14]. Here are the main characteristics of our setting.

- The linear size R of the objects is determined by the lattice size $H \times V$.
- All N_Δ 's considered for the averages characterize objects spanning the whole lattice. These objects might not be the largest among all loops but, with high probability, will be among the largest. In a sense, they describe only percolating objects.
- Also with high probability, the objects will bounce more than once on the boundary. They will therefore probe both the bulk and the boundary and hence carry information about the conditions of both regions.

It is interesting to recall the main features of the other simulations [13, 14] alluded to above and contrast them with those of ours.

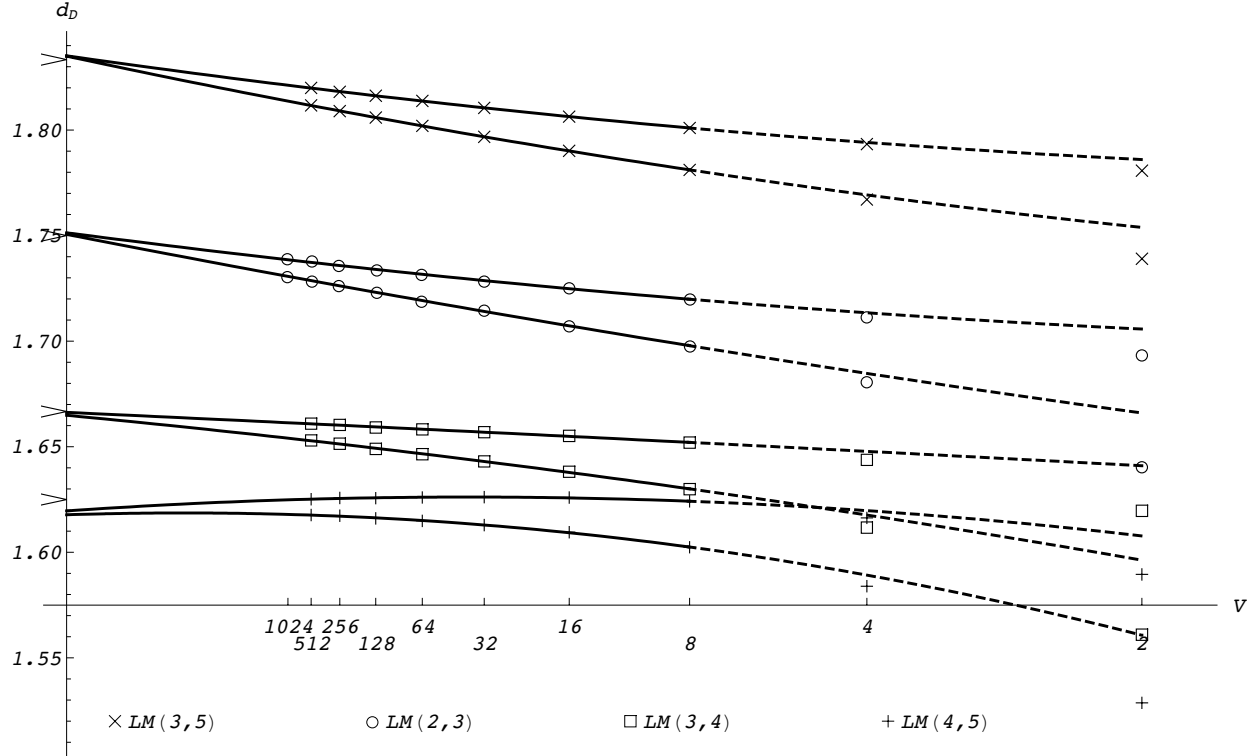


Figure 2: The data $\{d_{D,1}^{H \times V}\}$ (lower curve) and $\{d_{D,2}^{H \times V}\}$ (upper curve) for the four models studied. The curves are the fits obtained as described in Section 3.2.2, to which end only lattices with $H \times V \geq 9 \times 8$ are used. Here and throughout the paper, the error bars are much smaller than the symbols used to depict the data.

model	κ	$d_D^{\text{theo}} = 1 + \frac{\kappa}{8}$	$\widehat{d_{D,1}}$	$\widehat{d_{D,2}}$
$\mathcal{LM}(3,5)$	$\frac{20}{3}$	$\frac{11}{6} \sim 1.833\dots$	1.835 1	1.835 1
$\mathcal{LM}(2,3)$	6	$\frac{7}{4} = 1.75$	1.75059 62	1.75133 58
$\mathcal{LM}(3,4)$	$\frac{16}{3}$	$\frac{5}{3} \sim 1.667\dots$	1.665 1	1.666 1
$\mathcal{LM}(4,5)$	5	$\frac{13}{8} = 1.625$	1.618 1	1.620 1

Table 2: Values $\widehat{d_{D,1}}$ and $\widehat{d_{D,2}}$ with 95%-confidence intervals.

Asikainen *et al* [13] perform measurements on a single square lattice of linear size 4096. In fact, they use two sets of measurements as they probe both open and periodic boundary conditions. They consider all FK graphs contained in a configuration. For each of these graphs, they calculate both its mass (the equivalent of N_Δ above) and its gyration radius. The masses of all FK graphs of all configurations having their radius in a given window $[R_i, R_{i+1}]$ will contribute to this linear size bin. The characteristics of their setting are the following.

- The linear size R depends on the FK graph being studied, not on the lattice.
- All objects of every size in a configuration are considered.
- Smaller FK graphs may completely avoid the boundary and probe only the bulk. In the open boundary case, larger ones are likely to explore regions close and far from the boundary.

While our approach is close in spirit to the growth process described by SLE, one can say that the study by Asikainen *et al* concerns global statistical features of FK graphs.

The simulations carried out by Janke and Schakel [14] are limited to the Ising model but aimed at clean measurements. Like us, they perform measurements on several lattices. These are all square and their linear sizes range from 8 to 512. They measure both spin and FK clusters and, for each type of cluster, they count the number of sites occupied by the objects. This is a natural thing to do for spin clusters, but perhaps a little less natural for FK clusters. Contrarily to the Asikainen collaboration and us, they do not tackle directly the fractal dimensions of the objects they study. Instead, they extract the fractal dimensions from the *percolation strength* P_∞ (the fraction of sites in the largest cluster) and the average cluster size χ . This trick allows them to obtain very clean values for the fractal dimensions they measure from relatively small lattices. In summary, their setting is characterized by the following.

- The properties (P_∞ and χ) are studied as functions of the linear size of the lattices.
- P_∞ probes one particular object, similar, yet not equal, to the defect we are concentrating on. The observable χ is an average over all clusters.
- They use only periodic boundary conditions and therefore all their objects are in the bulk.

As one can see, the three experiments (Asikainen *et al*'s, Janke and Schakel's, and ours) are quite different. The fact that they nevertheless give very similar results is an indication that the physical observables considered are rather robust, with variations in boundary conditions or even definitions not causing major differences between measured fractal dimensions. There is no doubt, however, that the speed of convergence to asymptotic behaviour obtained by Janke and Schakel is impressive. We note that an earlier paper, that of Fortunato [29], also reports the cluster mass for the Ising and the 3-Potts models for the *spin clusters*. For the Ising model, Fortunato reproduces the predicted value ($\frac{187}{96}$ that appears in Table 1) to four significant digits. For his measurements, he uses only the largest cluster in a configuration; this is not exactly what we do (ours always "percolate" from top to bottom but they might not be the largest) but his setting is nevertheless the one closest to ours.

3.2 Technical issues

3.2.1 Probability distribution of $d_D^{H \times V}$ and error on measurements

The most obvious way of estimating¹ $d_D^{H \times V}$ is

$$\widehat{d_{D,1}^{H \times V}} = \frac{1}{|S|} \sum_{\sigma} \frac{\log N_{\Delta}(D_{\sigma}^{H \times V})}{\log R^{H \times V}} \quad (3.5)$$

where the sum runs over the sample S with sample size $|S|$, $R^{H \times V}$ is the total number of quarter-circles accessible to the defect (including those on the boundary), while $N_{\Delta}(D_{\sigma}^{H \times V})$ is the actual number of quarter-circles visited by the defect in the configuration $D_{\sigma}^{H \times V}$. For a defect entering at one corner of a rectangle and exiting near the opposite one, the number $N_{\Delta}(D_{\sigma}^{H \times V})$ is never zero and this definition works well. For other geometric objects to be studied in Section 4, however, a naive extension of this definition fails. For example, there are configurations $D_{\sigma}^{H \times V}$ whose number of red bonds is zero and the logarithm cannot be taken for this $D_{\sigma}^{H \times V}$. An alternative is

$$\widehat{d_{D,2}^{H \times V}} = \frac{\log \frac{1}{|S|} \sum_{\sigma} N_{\Delta}(D_{\sigma}^{H \times V})}{\log R^{H \times V}}. \quad (3.6)$$

¹We use " \hat{x} " to denote an estimate of the random variable x .

Under relatively mild hypotheses on the distribution of N_Δ , the two sets $\{d_{D,1}^{H \times V}\}$ and $\{d_{D,2}^{H \times V}\}$ should converge to the same d_D when the mesh of the lattice goes to zero, that is, when $R^{H \times V} \rightarrow \infty$. The rates of convergence, on the other hand, may of course differ.

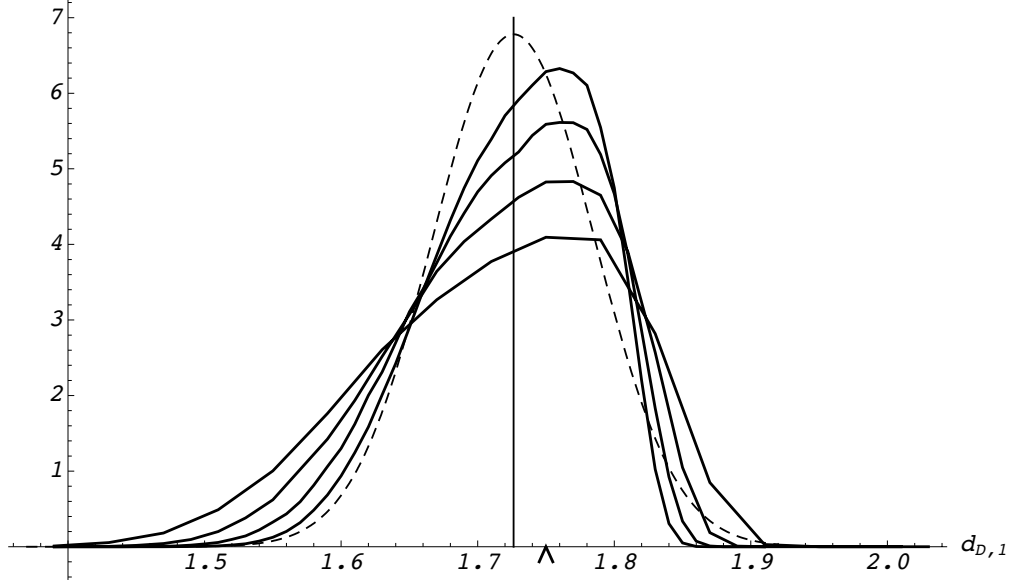


Figure 3: Probability density functions (pdf) for $d_{D,1}^{H \times V}$ for $H \times V = 33 \times 32, 65 \times 64, 129 \times 128$ and 257×256 . The dashed curve represents the pdf of the normal distribution with same mean and variance as the distribution for $d_{D,1}^{257 \times 256}$.

The probability distribution function (pdf) for $d_{D,1}^{H \times V}$ for critical percolation is shown in Figure 3 for four sizes of the lattice. The narrower distributions correspond to larger lattices (smaller mesh). The dashed curve is the normal distribution that has the same mean and variance as the distribution for $d_{D,1}^{257 \times 256}$. Up to an affine transformation, the distribution of $\log N_\Delta$ is the same as that of $d_{D,1}^{H \times V}$. If the lattice model at $\beta = 1$ indeed has SLE_6 as its scaling limit, the Hausdorff dimension should be $\frac{7}{4}$ by Beffara's theorem (2.2). The figure does not exclude this, but the convergence toward the Dirac mass $\delta(d_D - \frac{7}{4})$ is rather slow. Even for $H \times V = 257 \times 256$, $\log N_\Delta / \log R$ is likely to take any value between 1.6 and 1.8. The standard deviation is therefore large for $d_{D,1}^{H \times V}$ and consequently for $\log N_\Delta$. Note finally that, even though the pdf for $d_{D,1}^{H \times V}$ is skewed to the right, the window $[\widehat{d_{D,1}^{H \times V}} - 2s, \widehat{d_{D,1}^{H \times V}} + 2s]$, where s is the standard deviation of the sample, is a fair approximation of the 95%-confidence interval. To determine the confidence interval for $\widehat{d_{D,2}^{H \times V}}$, we first compute it for $\widehat{N_\Delta}$ and then take the log of both extremities of the interval. Taking the log should make the interval asymmetrical with respect to the mean. However, the intervals are small and this asymmetry can be ignored when estimating the confidence interval.

Table 3 contains information on the confidence intervals for critical percolation $\mathcal{LM}(2, 3)$ and the logarithmic tricritical Ising model $\mathcal{LM}(4, 5)$. As discussed in Appendix B, critical percolation is the fastest to simulate and we have large samples. The logarithmic tricritical Ising model, on the other hand, is the slowest that we have studied and samples are considerably smaller. One can see that the confidence intervals for $\widehat{d_{D,1}^{H \times V}}$ and $\widehat{d_{D,2}^{H \times V}}$ are essentially identical. Note that the precision of measurements are very good with five or six significant digits. For our purposes, however, they are only acceptable. Indeed, suppose again that Beffara's result applies to the thermodynamic limit of these lattice models. Then, around $H \times V = 257 \times 256$, $d_{D,1}^{H \times V}$ remains more than 0.03 away from $d_D = \frac{7}{4}$ for $\mathcal{LM}(2, 3)$ (resp. 0.07 away from $d_D = \frac{13}{8}$ for $\mathcal{LM}(4, 5)$), but between $H \times V = 257 \times 256$ and 513×512 , this gap has been reduced only by 0.002 (resp. 0.00032). The large variance and the slow progress of the mean towards the asymptotic value of

d_D make this measurement difficult. As the authors of [13] point out: “The asymptotic power law dependence of the various masses on R is approached relatively slowly.”

This makes the extrapolation $H, V \rightarrow \infty$ not only necessary but also delicate. How we perform this extrapolation is the topic of Paragraph 3.2.2.

			$\mathcal{LM}(2, 3)$			$\mathcal{LM}(4, 5)$	
H	V	S	$\widehat{d_{D,1}^{H \times V}}$	$\widehat{d_{D,2}^{H \times V}}$	S	$\widehat{d_{D,1}^{H \times V}}$	$\widehat{d_{D,2}^{H \times V}}$
3	2	5000000	1.64071 08	1.69283 07	100000000	1.52870 06	1.58952 06
5	4	1000000	1.68060 36	1.71113 33	100000000	1.58394 04	1.61629 04
9	8	1000000	1.69777 27	1.71982 25	50000000	1.60240 03	1.62413 04
17	16	1000000	1.70754 21	1.72500 20	10000000	1.60952 06	1.62595 06
33	32	1000000	1.71396 18	1.72856 17	20000000	1.61291 04	1.62614 04
65	64	1000000	1.71915 15	1.73164 15	2201000	1.61489 10	1.62598 10
129	128	1000000	1.72312 13	1.73399 12	206000	1.61609 27	1.62564 27
257	256	1000000	1.72624 12	1.73588 11	229700	1.61732 22	1.62574 23
513	512	1000000	1.72867 11	1.73731 10	64400	1.61764 38	1.62513 38
1025	1024	1000000	1.73074 09	1.73855 09			

Table 3: $\widehat{d_{D,1}^{H \times V}}$ and $\widehat{d_{D,2}^{H \times V}}$ with confidence intervals for two of the models. The notation 1.64071|08 means that the 95%-confidence interval is 1.64071 ± 0.00008 .

3.2.2 Extracting $\widehat{d_D}$ from $\{\widehat{d_{D,1}^{H \times V}}\}$ and $\{\widehat{d_{D,2}^{H \times V}}\}$

By definition of the fractal dimension, the number of quarter-circles N_Δ visited by the defect is proportional to R^{d_D} . Therefore, for sufficiently large R , one may assume that

$$\frac{\log N_\Delta}{\log R} \approx d_D + \frac{a}{\log R} \quad (3.7)$$

where a is another constant to be determined from the data. The approximation (3.7) is linear in $(\log R)^{-1}$ and a simple linear fit should be sufficient. However, the curves in Figure 2 clearly show that the sizes of the lattices we work with are too small for (3.7) to be a reasonable fit.

A better approximation is proposed in [30] where a renormalisation group analysis leads to

$$\frac{\log N_\Delta}{\log R} \approx d_D + \frac{a}{\log R} + \frac{b}{R^\theta \log R} \quad (3.8)$$

where a, b are constants to be fitted and θ is a known exponent depending on the model. It is $\frac{4}{3}$ for the Ising model, for example. Using (3.8) adds a hypothesis on the scaling behaviour of the model, that of the renormalisation group. Even though we did explore the quality of the fit obtained with (3.8), we use the following linear fits to get d_D :

$$\frac{\log N_\Delta}{\log R} \approx \sum_{i=0}^k a_i \frac{1}{(\log R)^i} \quad (3.9)$$

where the parameter a_0 is to be interpreted as \widehat{d}_D . The number k of terms in the fit is chosen somewhat heuristically by requiring that the p -value² for each a_i remains below 0.05 and that k be the same for all models. We find that $k = 2$ is best for our data.

Let us summarize some typical p -values obtained for fits of $\widehat{d}_{D,i}^{H \times V}$ when the fits are based on all lattices but the two smallest ones: 3×2 and 5×4 . In fits with functions 1 and $\frac{1}{\log R}$, the p -values of the coefficient of 1 is always smaller than 10^{-14} and that of the coefficient of $\frac{1}{\log R}$ is smaller than 4×10^{-4} , except in one case in which it is ≈ 0.3 . When three functions are used, 1, $\frac{1}{\log R}$ and $\frac{1}{(\log R)^2}$, the p -values of the coefficients remain small: less than 10^{-11} for the coefficient of 1 and less than 0.05 for that of $\frac{1}{\log R}$. For that of $\frac{1}{(\log R)^2}$, the p -value is also very small < 0.02 for all fits except those for the Ising model. That means that, for the logarithmic Ising model, the quadratic term might not be necessary. Indeed, in Figure 2, the curves for the logarithmic Ising model are seen to be exactly those where the concavity of the fit flips from being upward to downward implying that the coefficient of the quadratic term must be very close to zero. Finally, fits including a fourth term, $\frac{1}{(\log R)^3}$, have p -values larger than 0.1 for many of their coefficients, not only for the added term.

We reject the values $\widehat{d}_{D,i}^{H \times V}$ obtained for the smallest lattices. To choose which ones to reject, we proceed as follows. We reject the lattices whose inclusion (or rejection) cause a major change in the quality of the fit. Keeping the lattice $H \times V = 9 \times 8$, but rejecting the smaller ones, seems to be optimal. An indirect confirmation of this choice comes from the hypothesis that Beffara's theorem is valid for our lattice in the case of critical percolation. We also have to choose R . In the definition of the Minkowski dimension, R is the linear size of the box superimposed on the defect. An initial choice could therefore be the square root of the total number of quarter-circles: $\sqrt{2H \times V}$. However, the defect has access also to the half-circles on the boundary. A better choice is therefore the square root of the number of quarter-circles that can be occupied by the defect. In the present geometry, this is

$$R = \sqrt{2H \times V + 4V} \quad (3.10)$$

and this is the definition we use. This choice should not have a significant impact if large lattices are considered. For the sizes considered here, though, there is an effect, as discussed below. The values reported in Table 2 are those obtained with (3.10) and $k = 2$ for both sets $\{\widehat{d}_{D,1}^{H \times V}\}$ and $\{\widehat{d}_{D,2}^{H \times V}\}$ based on lattices with $H \times V \geq 9 \times 8$ only. Using (3.8) for the logarithmic Ising model gives $\widehat{d}_{D,1} = 1.6693$ and $\widehat{d}_{D,2} = 1.6652$; the quality of these results is comparable to the values in the table, but no better. As we shall see shortly, the limitation is clearly the errors on the $\widehat{d}_{D,i}^{H \times V}$ for large $H \times V$ and the choice of definition for the parameter R .

We have explored also the possibility of predicting, from our data, both the fractal dimension d_D and the exponent of the correction term proposed by (3.8). If the correction term is small, this amounts to a nonlinear fit for the parameters a_i in

$$N_\Delta = R^{a_0} a_1 \left(1 + \frac{a_2}{R^{a_3}} \right). \quad (3.11)$$

But we have only 10 lattices (11 for critical percolation) for 4 parameters. The Levenberg-Marquardt method (see [31], for example) does provide an excellent fit (in the sense that the curve is very close to the data), but the exponent d_D and θ are totally off. Asikainen *et al* say that they use bins $[R_i, R_{i+1}]$ with $R_{i+1} = \sqrt{2}R_i$. This gives them more than twenty data points. Still, like us, they claim that the prediction of the correction exponents is impossible with their range of data. We abandoned this idea.

To evaluate the statistical error on the reported values $\widehat{d}_{D,1}$ and $\widehat{d}_{D,2}$, we perform the following simulation. We add noise to each datum of either set $\{\widehat{d}_{D,i}^{H \times V}\}$, $i = 1, 2$, distributed normally with zero mean and variance equal to the standard deviation measured from the previous experiment (see Figure 3). With this new set of "noisy" data, we work out the fit as described above. Repeating this experiment a large number

²In a linear regression as the present ones, the p -value associated with one of the coefficients in the fit tests the hypothesis that this coefficient is zero. Therefore, a p -value of 0.05 for the coefficient c means that one might erroneously reject the hypothesis that c is zero in 5% of the cases.

of times (1000) gives a good idea of the deviation on $\widehat{d_{D,1}}$ or $\widehat{d_{D,2}}$. For the best data, i.e. those for critical percolation, the noise coming from the width of the probability distribution of N_Δ amounts to an error (= 95%-confidence interval) of 0.0006 on either $\widehat{d_{D,1}}$ or $\widehat{d_{D,2}}$. This is the error quoted in Table 2. We stress that this is the statistical error. But this method of evaluating the statistical error also gives an impression of the sensitivity of the measurements $\widehat{d_{D,1}}$ and $\widehat{d_{D,2}}$ on a single datum. We have repeated this experiment by changing *one* datum, that on the largest lattice $H \times V = 1025 \times 1024$, to the value at either extremity of its confidence interval. This changes $\widehat{d_{D,i}}$ by a little more than two units of its fifth significant digit. In other words, the normal statistical error on a single datum leads to an error about a fourth of that on the whole set. This justifies our claim that the errors on the data for $d_{D,i}^{H \times V}$ significantly limit the precision on the $\widehat{d_{D,i}}$'s. Of course, it would be nice to probe lattices whose linear size is a few order of magnitude larger than the ones allowed by our slow MC algorithms.

lattices used	2 to 16	4 to 32	8 to 64	16 to 128	32 to 256	64 to 512	128 to 1024
$\widehat{d_{D,2}}$ with R	1.73484	1.74220	1.75013	1.75433	1.75113	1.74988	1.74999
$\widehat{d_{D,2}}$ with R'	1.74210	1.74430	1.74961	1.75348	1.75115	1.75003	1.75004

Table 4: Measurements $\widehat{d_{D,2}}$ for critical percolation $\mathcal{LM}(2,3)$ obtained from a subset of the $d_{D,2}^{H \times V}$.

Janke and Schakel [14] report an interesting feature of their data for the Ising model. Their measurement of the dimension of the FK hull, the one to be compared with our dimension of the defect, shows the following behaviour. When they limit their analysis to their smaller lattices ($L = 8$ to 48), the dimension obtained is 1.665, very close to the predicted $d_D^{\text{Ising}} = \frac{5}{3}$. But when they use their largest one ($L = 64$ to 512), the result seems to slip down a little (to 1.641). This is obviously a small effect. It should be noted that they report results, for this mass, only with the average cluster size χ . In Table 4, we report the values $\widehat{d_D}$ for critical percolation obtained from the set $\{d_{D,2}^{H \times V}\}$ by extrapolation from 4 consecutive lattices. For example, the first fit is that with $H \times V = 3 \times 2$ to 17×16 . (We admit, of course, that using 4 data for a 3-parameter fit is not ideal.) The results of the upper line use the definition (3.10) of R as $\sqrt{2H \times V + 4V}$, the definition used throughout this analysis. These first move up and even overshoot the theoretical value, but then come back to extremely good ones. The problem reported by Janke and Schakel is not seen here. As underlined in Section 3.1, our settings are different. Our defect always crosses diagonally the lattice and one could guess that its gyration radius is fairly uniform. It remains to be seen how this could be an advantage. Note that we perform their experiment with our data for *critical percolation* as these go to $V = 1024$. The same experiment done for our data for the logarithmic Ising model show the same behaviour (including the overshoot and the final improvement of estimates when using larger lattices). Table 4 is completed by results done with respect to another definition of R, namely $R' = \sqrt{2H \times V}$. Although this change hardly alters the fits on large lattices, it has an important effect on fits with small ones. This is to be expected. It nevertheless demonstrates how sensitive the extrapolation is to the definition of R. For the fits reported in Table 2, the switch from R to R' leads to a change in $\widehat{d_D}$ within the confidence interval for all models but the logarithmic tricritical Ising model $\mathcal{LM}(4,5)$ where it is responsible for an increase twice as large as this interval. This indicates that, for the lattice sizes studied, there is no use trying to extract better extrapolations from our data, unless one can choose an R on a more theoretical basis.

3.2.3 Importance of boundary half-circles

In [32], the role of boundary conditions as described by defects is studied for critical dense polymers $\mathcal{LM}(1,2)$. The half-circles that are added along the boundary of the domain obviously change the probability of the configurations. For example, if $\beta > 1$, configurations with many loops are favoured and those with several (shorter) paths joining two points of the boundary will be common. However, for critical percolation that has $\beta = 1$, one may think that these half-circles do not play any role. This is not so. Configurations with and without these half-circles will have noticeably different d_D .

Consider a long cylinder whose circular section contains an odd number of boxes. There will be (at least) one defect going from one end of the cylinder to the other. The boundary of the cylinder is now the union of two circles. The paths reaching these boundary circles can all be closed by boundary half-circles, all but one. Or they can be left open. In configurations without half-circles, the loops starting and ending at the boundary will be as many open loops competing for space near the boundary. The defect that crosses the cylinder will in this case be less dense close to the boundary. If, however, half-circles are added, they can be used by the defect to fill the space close to the boundary. Consequently, the dimension d_D of the defect measured on configurations without half-circles will be smaller than that measured on configurations with them. The latter is probably independent of the geometry. The former is likely to depend on it; for example, d_D depends on the length of the cylinder (without half-circles) and tends to d_D (measured with half-circles) when the ratio length/circumference tends to infinity. This interpretation is consistent with the growth process that is described by SLE. When an SLE_6 interface is grown on, say, the half-plane, it is allowed to bounce on the real axis (the boundary). The loop gas configurations with half-circles at the boundary are those allowing this reflection of the defect on the boundary.

$\langle \# \text{ of intersections of defect} \\ \text{with one line of boxes} \rangle / (2H)$

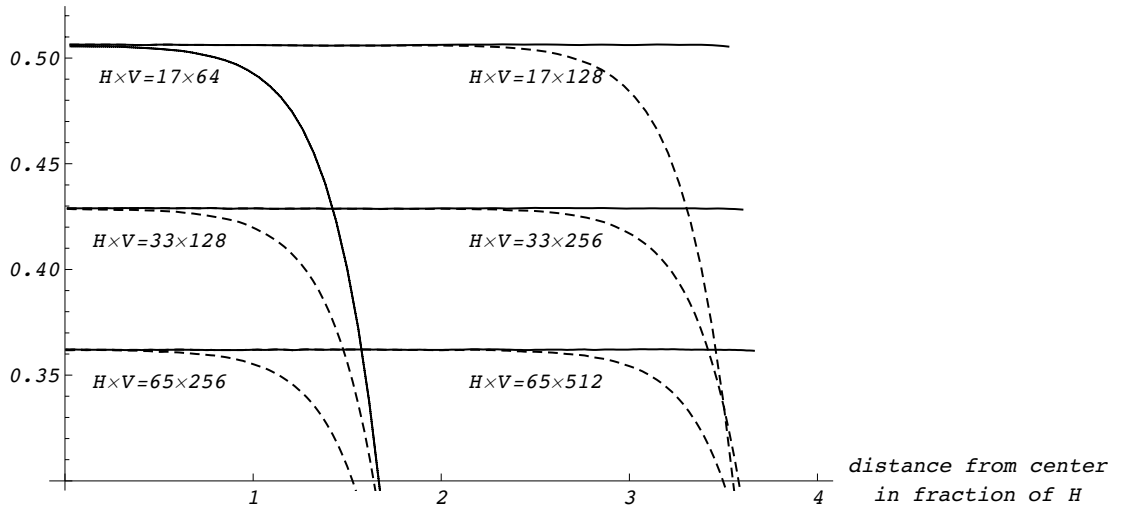


Figure 4: Density of the defects on six cylinders as a function of the position along the cylinder axis. Boundary conditions are without (dashed curves) or with (full curves) half-circles.

This effect of half-circles at the boundary can be seen in simulations even on long cylinders. In Figure 4, we plot the average of the ratio

$$\frac{\# \text{ of quarter-circles visited by the defect}}{\text{total \# of quarter-circles}} \quad (3.12)$$

for each row of boxes along the cylinder. This ratio drops sharply near the boundary of the cylinder when half-circles are absent (dashed curves on the graph). When they are present (straight curves), the ratio is essentially constant on the full length of the cylinder. (The sizes given on the figure are labelled $H \times V$ where

H stands for the number of boxes along a section and V for the length of the cylinder.) The two ratios (with or without half-circles) differ significantly over a distance from the extremities that is about the length of the circumference.

4 Other geometric objects: hull, cluster mass, external perimeter and red bonds

4.1 Definition of masses for loop gas clusters

The classical definitions of the various masses (cluster mass, hull, external perimeter and red bonds) need to be adapted to the context of a loop gas whose thermodynamical limit for rational κ is argued to be a logarithmic minimal model. This extension is necessary as the random variables are not spins but boxes with only two states. It may provide a larger domain of exploration as the loop gas is parametrized by the continuous parameter κ and not only an integer, like the Q-Potts models.

Figure 5 (a) gives a configuration of the Ising model on a rectangular lattice. The reason for drawing it obliquely will become clear below. A configuration of FK clusters is obtained from this spin configuration as follows. Bonds between spins of distinct signs are erased and bonds between identical spins are removed (resp. kept) with probability $(1 - p)$ (resp. p) where $p = 1 - e^{-\alpha}$ for α the inverse of the temperature and the Ising Hamiltonian of the form $H = - \sum_{\langle ij \rangle} (\delta_{\sigma_i \sigma_j} - 1)$. Figure 5 (b) shows a configuration obtained this way from the spin configuration in Figure 5 (a). The first step of a Swendsen-Wang upgrade consists precisely in constructing an FK configuration from a spin configuration. An FK configuration is partitioned uniquely into FK clusters, the maximal connected components of bonds and sites. We now recall the definitions of the various masses for these clusters. We shall concentrate on the largest cluster, the one shown in dark in Figure 5 (c). To distinguish between the classical definitions of these masses and the new ones to be introduced here, we add the label “spin” to the former and “loop” to the latter.

The *spin cluster mass* is the number of sites connected by the bonds of the FK cluster. A site from the cluster belongs to the *spin hull* if a continuous curve can be drawn from this site to infinity (the boundary of the lattice) without crossing any of the cluster bonds. The *spin hull* is marked by pale (yellow) squares in Figure 5 (d) and the other vertices of the cluster by dark (blue) squares. The *spin hull mass* is the number of sites in the spin hull, that is, the number of yellow squares. The hull partitions the whole lattice into three disjoint sets of sites: the hull itself, its interior and its exterior. Its interior consists of the sites of the lattice not belonging to the hull and from which there are no continuous paths to infinity avoiding all cluster bonds. The interior of the hull contains sites belonging to the FK cluster (drawn in dark (blue)) and others that do not. The exterior of a cluster is the complement of the union of the hull and its interior. The *spin external perimeter* (EP) is the subset of the exterior sites having at least one nearest neighbor in the hull. In Figure 5 (d), they are marked by dark circles (in green). The spin EP mass is the number of sites in the external perimeter.

The last set to be described is that of *spin red bonds* (RB). Among the sites of the FK cluster, identify those that have the largest vertical coordinate and, among these, call σ_{NW} the site with the smallest horizontal coordinate. Similarly, define as σ_{SE} the site with smallest vertical coordinate and, if there is more than one with this coordinate, the one among these with the largest horizontal coordinate. A bond in the FK cluster is a red bond if its removal breaks the FK cluster into two disconnected parts, each containing one of the two sites σ_{NW} and σ_{SE} . In other words, if a voltage difference is applied between σ_{NW} and σ_{SE} , the breaking of a single red bond will interrupt the electric current. The concept of a “red bond” is credited to Stanley. The definition appears in his paper [33] but not the name. If bonds are imagined as fuses, the first that will turn red (and burn) are the red bonds, hence the name. Note that the name “simply-connected bonds” is also used for the red bonds. This name is somewhat misleading as it does not have its usual topological meaning. It merely refers to the fact that these bonds keep the cluster connected. In the extension to *loop red bonds*, we shall apply the voltage difference between *all* topmost sites and *all* bottommost ones between the entry and exit points of the defects. This is a slight departure from the original definition that we have just introduced. The red bonds, obtained according to this new definition, are represented on Figure 5 (d) by small (red) slashes through them.

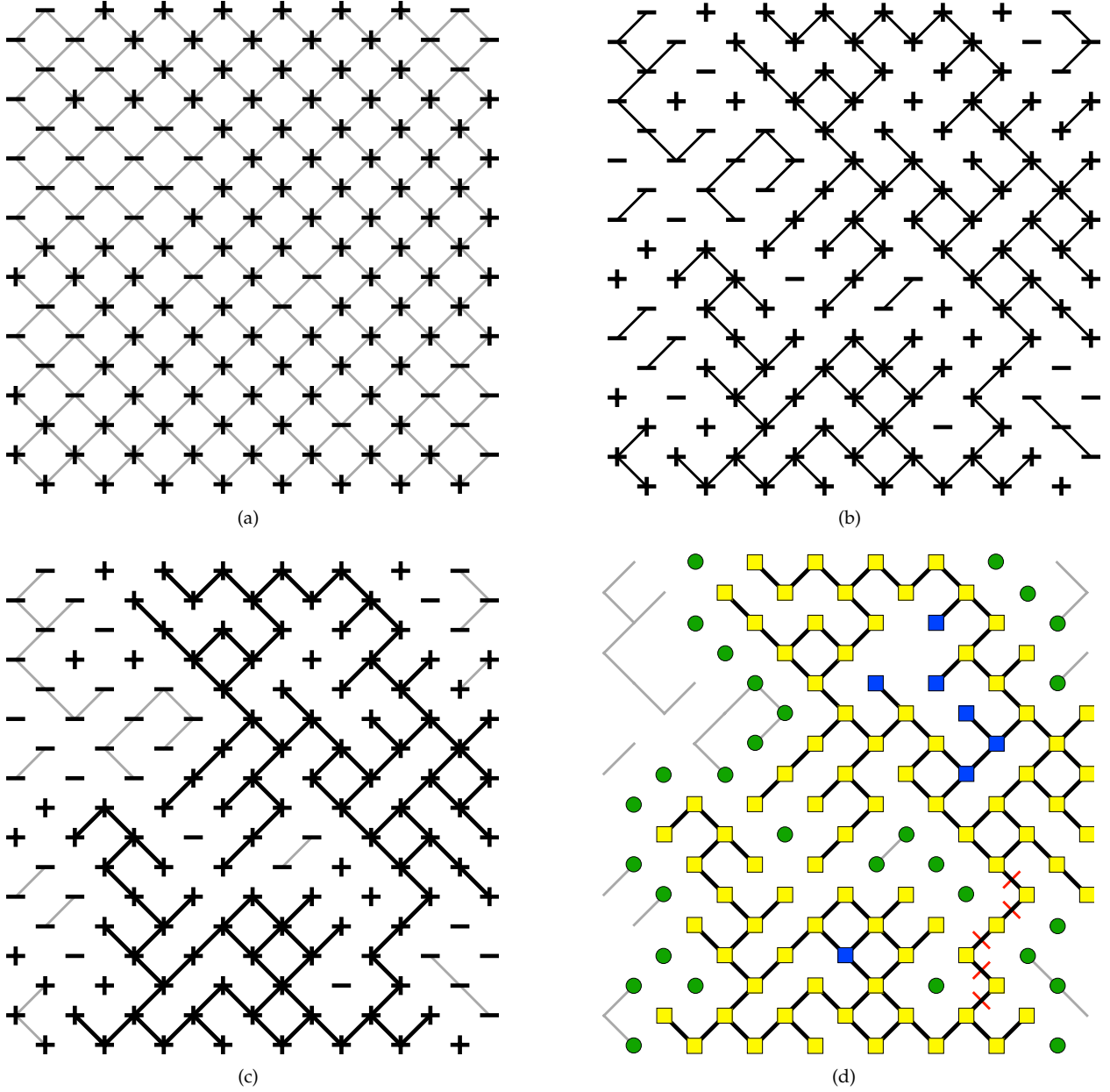


Figure 5: Four steps to construct various *spin masses* starting from a spin configuration.

The correspondence between an FK configuration (obtained from a spin configuration) and a loop gas configuration is one-to-one, once the boundary condition of the latter has been chosen. We superimpose a grid whose mesh is $1/\sqrt{2}$ times that of the spin lattice, as in Figure 6 (a). Spins of the first lattice occupy about half of the vertices of the new one. The state of each box in the loop gas configuration is determined from the FK configuration as follows. Two vertices of each box are occupied by spins. If there is a bond between these two sites in the FK configuration, the state of the box is such that the two quarter-circles do not intersect this bond. If there is no bond, then the two quarter-circles are drawn as if to prevent a bond to be drawn there. In such a loop configuration, the FK clusters not reaching the boundary are enclosed by loops as “tightly” as possible.

To construct the loop gas configuration corresponding to the FK configuration of Figure 5 (b), we choose a boundary condition where exactly *two* defects enter at the top of the lattice and exit at the bottom. All remaining boundary boxes are joined by half-circles between neighbouring boxes. The result is shown in Figure 6 (b). Again, we define the *loop masses* for the largest object (given by the defects), even though our definitions hold also for the closed loops themselves.

The geometric objects of the loop configuration, that we now propose to replace the classical (spin) masses by, are based only on the loop configuration and do not entail a choice of a compatible spin configuration (as one would in the second and last step of a Swendsen-Wang upgrade). They will *not* agree numerically with the spin masses of the original finite lattice but, hopefully, will have the same thermodynamical limit.

The *loop hull mass* of any closed loop is the number of quarter-circles of the loop, including the two quarter-circles of each boundary half-circle that the loop visits. The loop hull of a defect is defined similarly as the number of quarter-circles from its entry to its exit. The loop hull created by the two defects is shown in pale (yellow) in Figure 6 (c).

It is somewhat unfortunate that the word *hull* is used here as well as in the description of the SLE process, but with two different meanings. In SLE, the curve γ , which is the counterpart of a defect, is drawn, say, on the upper half-plane \mathbb{H} . There is no underlying lattice. The curve γ is allowed to touch the real line (the boundary of \mathbb{H}) and itself. The hull drawn by γ is the union of the points visited by γ with the set of all points that have been cut off from infinity (in \mathbb{H}) by the curve touching the real line or itself. The SLE hull is therefore likely to include open domains of various sizes. In the loop gas, the defect never touches itself as it is the union of disjoint quarter-circles. The best approximation of a tangency point occurs in boxes whose two quarter-circles are visited by the same loop (or defect). Between the two visits of such a box, the loop has circled a region in the lattice whose interior could be naturally identified with an open set. The quarter-circles of this open set *do not belong* to the loop hull mass. This is contrasted by their counterparts in the SLE setting which *do* belong to the SLE hull.

In the simulations, we will add the contributions of both defects, except for critical dense polymers with $\beta = 0$. Counting quarter-circles of both defects amounts to visualizing these two defects as left and right boundaries of a percolating cluster. For polymers, configurations with closed loops are forbidden. This means that the defects must visit every single quarter-circle of the lattice. Counting quarter-circles of both defects would then give the total number of quarter-circles for all (allowable) configurations and the fractal dimension of the loop hull mass would be exactly the predicted value, 2, and there is no need for simulations. Instead, we choose to restrict the counting to one of the two defects for this model ($\beta = 0$). This raises the question of whether the fractal dimension of defects depends on the number of macroscopic objects in the configuration, for example the number of defects crossing from top to bottom. This will be discussed in Section 4.3.3.

The definition of the *loop external perimeter* (EP) is inspired by Grossman and Aharony's biased walker [34]. When a loop intersects an edge, it does so perpendicularly and its direction at this intersection is therefore one of four choices: north, east, south and west. We start by constructing the loop EP of the left defect. At the top entry point of this defect, the direction is southward. Consider the box the loop is entering. If only one of the two quarter-circles of this box is visited by the loop (the defect), the external perimeter follows this quarter-circle. If *both* quarter-circles are eventually visited by the loop, the external perimeter will draw a quarter-circle leading to the edge on its left whether or not this quarter-circle belongs to the state of the box. The loop has now progressed to a new face visited by the loop. Its next step is chosen in the same left-biased way. The loop EP mass is defined as the number of quarter-circles visited by the left-biased walker following the left defect from its entry to its exit. As we are going to explore two other ways of defining the EP, we denote the one just described by EP1. An example of a hull is drawn in Figure 7 (a) and its external perimeter, according to definition EP1, appears in Figure 7 (b). Note that the hull of the left defect is part of or to the left of its external perimeter. As can be seen there, the external perimeter cuts out many of the inner meanderings of the hull. To use Janke and Schakel's words [15], it is a smoother version of the hull. Even though we have not measured the external perimeter of closed loops, we complete our definition EP1 for them. Find first the rightmost box edge crossed by the loop. If there is more than one such box, any of them will do. This edge is always horizontal. Starting from this edge with a southward direction, draw the EP by following a *right*-biased walker. Again, the hull will be part of or in the interior of the external

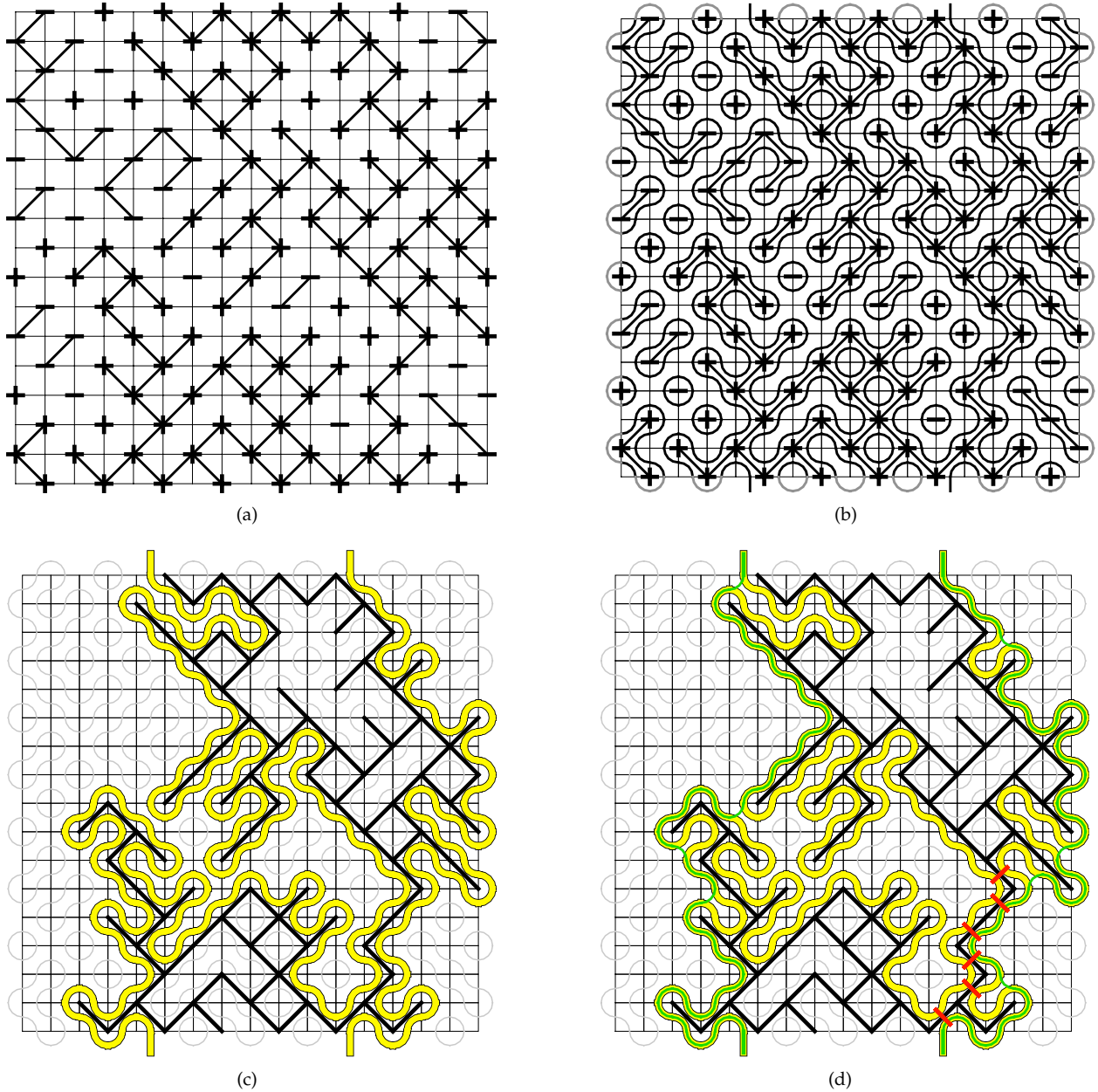


Figure 6: Four steps to construct *loop masses*.

perimeter. The mass of the loop EP is again the number of its quarter-circles. It is smaller (or equal) to the mass of the loop hull.

The next way of defining the external perimeter is closer to the interpretation of the two defects as enclosing a macroscopic FK cluster. In this interpretation both defects need to be considered and it is more natural to draw the EP for the left defect starting at the top and using a *right*-biased rule and then draw the EP for the right defect starting at its bottom and using again a *right*-biased rule. Figure 7 (c) gives the result for the hull in Figure 7 (a). Note that it is also the external perimeter given as an example in Figure 6 (d) in mid-gray (green) superimposed on the hull in pale gray (yellow). As we shall see, this new definition (EP2) works equally well for all models but one. The problematic model is again critical dense polymers,

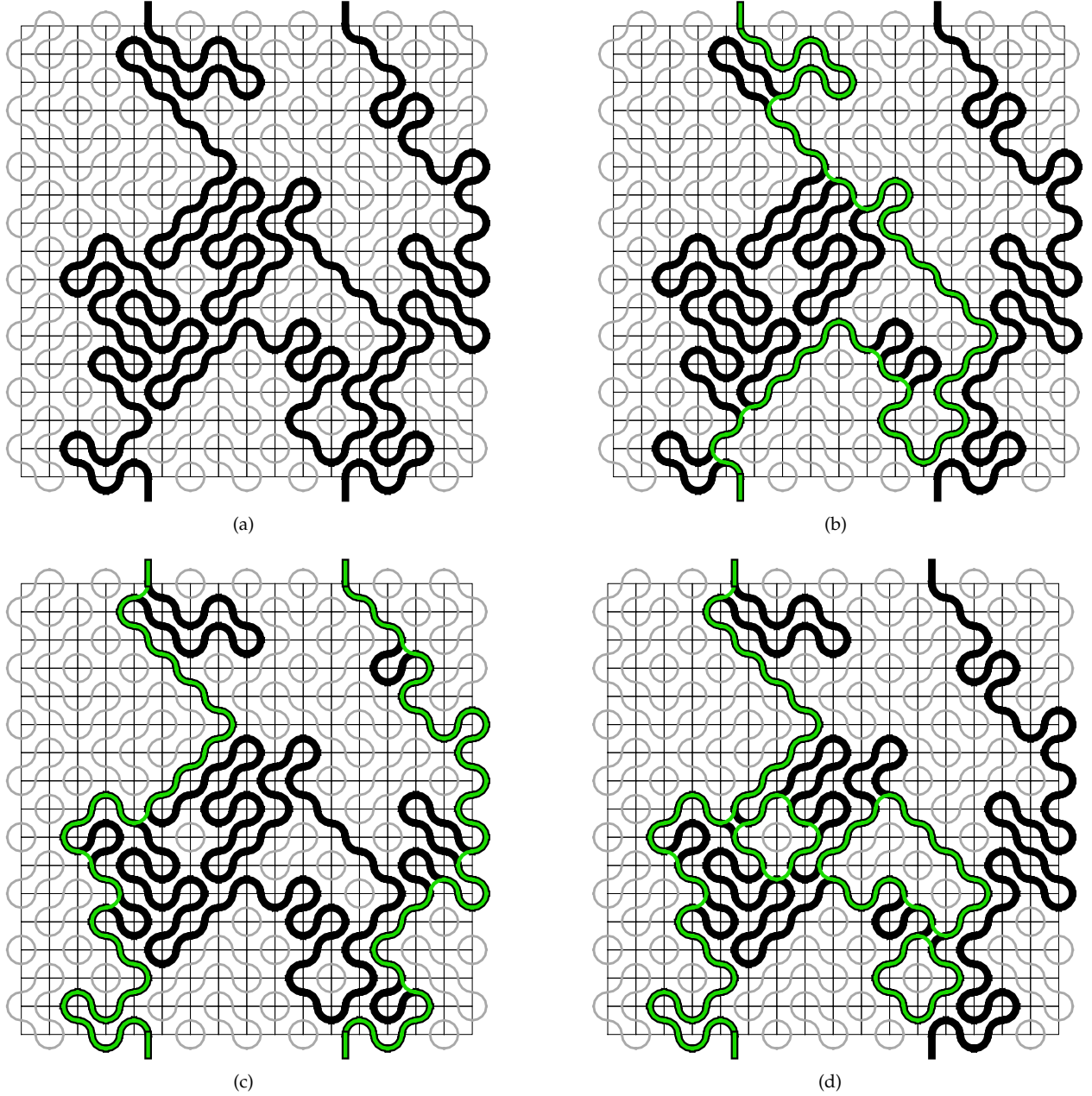


Figure 7: Three candidates for the *loop external perimeter*. Figure (a) shows the hull.

the “extreme model” with $\beta = 0$. As said before, the defects of this model fill the lattice. Using a right-biased rule to obtain the EP of the left defect would draw an EP wiggling along the boundary, using only the quarter-circles touching the boundary. Drawing the EP of the right defect starting from the bottom and using a right-biased rule would have the same effect. This would give the same number of quarter-circles for all configurations, and this number grows linearly with the (linear) size of the lattice. The resulting fractal dimension for polymers would be 1. This is not the predicted value and this definition does not probe the fractal nature of the geometric object.

Our final proposal for defining the loop EP is denoted by EP3 and consists in adding the “inner bubbles”.

The spin EP naturally adds sites that can be “deeply enclosed” within the cluster under consideration. Figure 5 (d) shows some of these bubbles. Indeed, besides the dark (green) disks to the left and to the right of the cluster, there is a handful of these disks trapped inside the cluster. We explore with EP3 the possibility of adding their counterparts in the loop gas case. Their addition requires several sweeps of the left- (or right-)biased algorithm. For example, after having drawn the external perimeter with, say, the right-biased definition for the left defect, we look for boxes visited by the hull but not by the EP just drawn. From those, we retain only boxes where one of the quarter-circles is not visited by the hull and where this quarter-circle is connected to the left lattice boundary by a path not intersecting the hull. Starting from this quarter-circle, we draw the right-biased EP of this “inner bubble”. Figure 7 (d) shows the resulting EP, with three “inner bubbles”. As we shall see in Section 4.3.2, this last definition EP3 *does not* converge to the predicted value d_{EP} but, instead, seems to converge to d_H .

A loop gas configuration is a choice of state for each box of the lattice and these states draw loops, not clusters. To define clusters from these loops and subsequently a *loop cluster mass*, we first define an *open bond*. The original spin lattice has spins on only (about) half of the vertices of the loop lattice. We say that a box of a loop configuration has (or draws) an open bond if its quarter-circles *do not* intersect the segment joining the two vertices of the original lattice. Maximally connected sets of bonds are clusters and the *loop cluster mass* of such a component is the number of open bonds. This is similar to clusters in bond percolation from which the name “open bond” is borrowed. When the boundary condition allows for defects, we define the cluster between two (vertical) defects as the connected set of bonds between the two defects reaching both the top and bottom boundaries. This set is unique unless there is a closed loop located between the two defects and connecting both the top and bottom of the lattice. In the unlikely occurrence of such a loop, we would use the leftmost connected set of bonds. The cluster mass is the number of its bonds. The geometric object used to define the loop cluster mass coincides with that of the spin cluster mass. However, the loop cluster mass counts bonds instead of vertices.

Cutting a bond in the cluster inside a hull (as just constructed) amounts to flipping the state of the corresponding box. If one wants to break the cluster between two defects into two connected parts in such a way that the electric current from the top to the bottom is cut (as does the cutting of red bonds), this flipping of the box will have to change the two vertical defects into two defects, the first connecting the two entries at the top boundary, the second the two exits at the bottom boundary. This occurs if and only if one of the quarter-circles of the box being flipped belongs to the left defect and the other to the right one. We therefore define the *loop red bond mass* (or RB mass) as the number of boxes visited by both defects. As will be seen from Figures 5 (d) and Figure 6 (d), the two definitions used to draw the spin and loop red bonds almost coincide, the difference being of one extra loop red bond in this particular example.

4.2 Measurements

The first thing to choose is the appropriate definition of R . This linear size is related to the size ϵ of boxes in the Minkowski definition (3.1) and appears explicitly in our approximation (3.4). It counts how many geometric building blocks (quarter-circles, bonds, sites) the mass under consideration may occupy. The natural thing to do is therefore to use two distinct definitions of R , one for the hull and the external perimeter

$$R_1 = \sqrt{2H \times V + 2H + 2V - 4} \quad (4.1)$$

counting the number of quarter-circles, and one for the cluster and red bonds

$$R_2 = \sqrt{H \times V} \quad (4.2)$$

counting bonds in the lattice.

Figure 6 describes the setting of our simulations. Two defects enter from the top and exit from the bottom. Square lattices $H \times V$ are used with H a power of 2. For all models, the smallest lattice has $H = 8$. The largest lattice for critical dense polymers has $H = 128$, for critical percolation $H = 1024$, while for all other models, the largest lattice has $H = 256$. The left defect enters in and exits from column number $H/4 + 1$, while the right defect enters in and exits from column number $3H/4$. This choice leaves a quarter of the boxes to the left of the left entry point, and a quarter to the right of the right entry point. The algorithm

model	$\bar{\kappa}$	d_H^{theo}	\hat{d}_H	d_{EP}^{theo}	\hat{d}_{EP}	d_C^{theo}	\hat{d}_C	d_{RB}^{theo}	\hat{d}_{RB}
$\mathcal{LM}(1,2)$	2	2	2.000	$\frac{5}{4} = 1.250$	1.250	2	2.062	$\frac{5}{4} = 1.250$	1.258
$\mathcal{LM}(3,5)$	$\frac{5}{3}$	$\frac{11}{6} \sim 1.833$	1.833	$\frac{13}{10} = 1.300$	1.280	$\frac{77}{40} = 1.925$	1.946	$\frac{14}{15} \sim 0.933$	0.956
$\mathcal{LM}(2,3)$	$\frac{3}{2}$	$\frac{7}{4} = 1.750$	1.750	$\frac{4}{3} \sim 1.333$	1.326	$\frac{91}{48} \sim 1.896$	1.912	$\frac{3}{4} = 0.750$	0.768
$\mathcal{LM}(3,4)$	$\frac{4}{3}$	$\frac{5}{3} \sim 1.667$	1.667	$\frac{11}{8} = 1.375$	1.373	$\frac{15}{8} = 1.875$	1.892	$\frac{13}{24} \sim 0.542$	0.557
$\mathcal{LM}(4,5)$	$\frac{5}{4}$	$\frac{3}{8} = 1.625$	1.627	$\frac{7}{5} = 1.400$	1.380	$\frac{229}{160} \sim 1.869$	1.884	$\frac{17}{40} = 0.425$	0.432

Table 5: Fractal dimensions of d_H (hull), d_{EP} (external perimeter), d_C (cluster) and d_{SC} (simply-connected bonds). For critical percolation $\mathcal{LM}(2,3)$, better estimates are available in Section 4.3.

used ensures that the defect entering at the top left will exit at the top right or at the bottom left. The entry points account for 4 edges of the lattice boundary; all other edges are matched pairwise by half-circles with a nearest neighbour edge. We limit our samples to configurations with defects crossing from top to bottom, like the configuration shown in Figure 6. The size of these samples are of at least 2×10^5 for each lattice, usually much larger for smaller lattices. For all models but critical dense polymers, we use the definition EP2 of the external perimeter. For critical dense polymers, we use EP1.

The extrapolation is done as follows. For the hull mass, we do a fit with only 1 and $1/\log R$ as functions and using all lattices but the smallest 8×8 . Figure 8 shows that the two functions 1 and $1/\log R$ are indeed sufficient. The fact that the data for critical dense polymers follow a slope different from the slopes of the other models can be easily explained. Recall that, for critical dense polymers, the two defects together fill the whole lattice and that, consequently, we choose to count only the quarter-circles of the left defect for this model. If we would do the same thing for one of the other models, the average number of quarter-circles would, by symmetry, be approximately half of what we actually measure. Therefore, by using formula (3.6), we would obtain

$$d_H^{\text{new}} = \frac{\log \langle N_\Delta \rangle / 2}{\log R} = d_H - \frac{\log 2}{\log R} \quad (4.3)$$

as the new measurement of d_H . It turns out that, for all other models, the slope of the fit is smaller in absolute value than $\log 2$. This definition d_H^{new} would therefore lead to fits with slope of the same sign as that obtained for critical dense polymers. For the three other masses, d_{EP} , d_C and d_{RB} , one observes a clear departure from linearity. As an example, the five curves for the red bond masses are drawn in Figure 9. We therefore add a term $1/(\log R)^2$ in the fit. As for d_H , we reject the smallest lattice 8×8 and, for d_C , also the second smallest 16×16 . The results of the measurements, using (3.6), appear in Table 5.

The definition of *loop hull mass* that we have proposed is obtained from the number of quarter-circles visited by the two defects crossing the lattice from top to bottom. It is thus equal to the fractal dimension d_D measured in Section 3.1 if the object is the union of both defects crossing from top to bottom. If we are willing to accept that, in the thermodynamical limit, these two defects have minimal effect on one another, then d_H should indeed be equal to d_D . This is confirmed by our simulations, and the hull is seen to have the best numerical estimate of the four masses considered here. This point will be discussed again in Paragraph 4.3.3. The agreement is less spectacular for the three other masses: d_{EP} , d_C and d_{RB} . For these three, there seems to be a systematic error: the estimates for d_{EP} are always smaller than the predicted one, and those for d_C and d_{RB} always bigger. It is for d_C that the discrepancies are most obvious, especially because the five models considered have their predicted values all grouped in the narrow interval $[1.86, 2]$. For example, \hat{d}_C^{Ising} is closer to the d_C^{theo} for critical percolation than the one for the logarithmic Ising model.

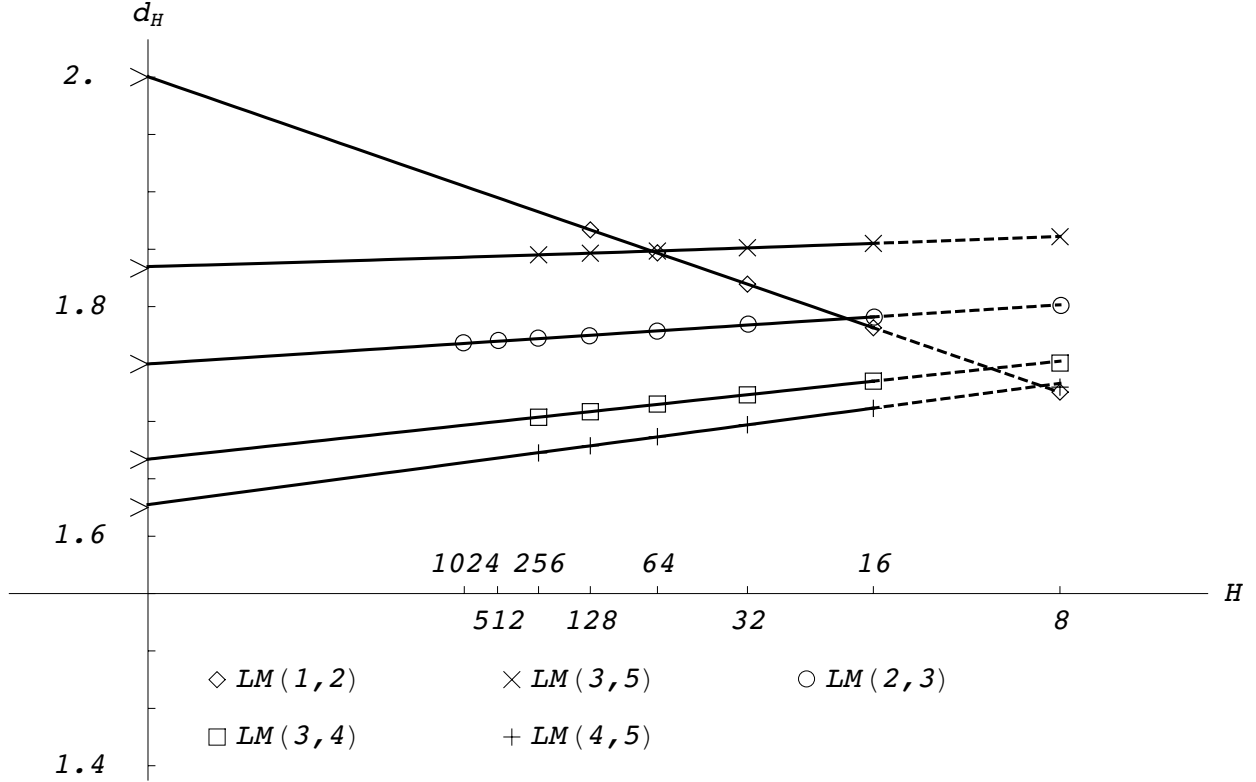


Figure 8: Measurements of d_H for the five models.

In Paragraph 4.3.1, we argue that these discrepancies stem mainly from the small lattices our slow upgrade algorithms allow us to consider.

4.3 Technical issues

4.3.1 Estimates of critical percolation masses from smaller data windows

As said before, we choose to reject the same lattices and use the same set of fitting functions for all models to obtain a given mass. But bigger lattices are accessible for critical percolation and better estimates for this model can therefore be obtained than those reported in Table 5. As we have done in Paragraph 3.2.2, we compute estimates \hat{d} of the various masses from a window of only 4 lattices. For the four masses d_H , d_{EP} , d_C and d_{RB} , we choose to restrict the fit functions to 1 and $1/\log R$. The results are contained in Table 6. Only estimates using (3.6) are reported. The agreement with theoretical values is better than reported in Table 5, significantly so for all but d_H . These improvements support the hypothesis that agreement with predicted values could be improved also for other models by using larger lattices and, therefore, that the proposed definitions for *loop* masses have the same thermodynamical limit as their *spin* counterparts.

Figure 10 shows the data for the four masses together with the fits obtained from the four largest lattices.

4.3.2 The definitions of the loop external perimeter

In Section 4.1, we proposed three definitions of the *loop external perimeter* that appeared to be natural extensions of its spin counterpart. The first, EP1, counts the number of quarter-circles visited by a left-biased walker starting its journey at the top of the left defect and ending when this defect exits the lattice. The second, EP2, uses the quarter-circles visited by a right-biased walker traveling both defects, the left one

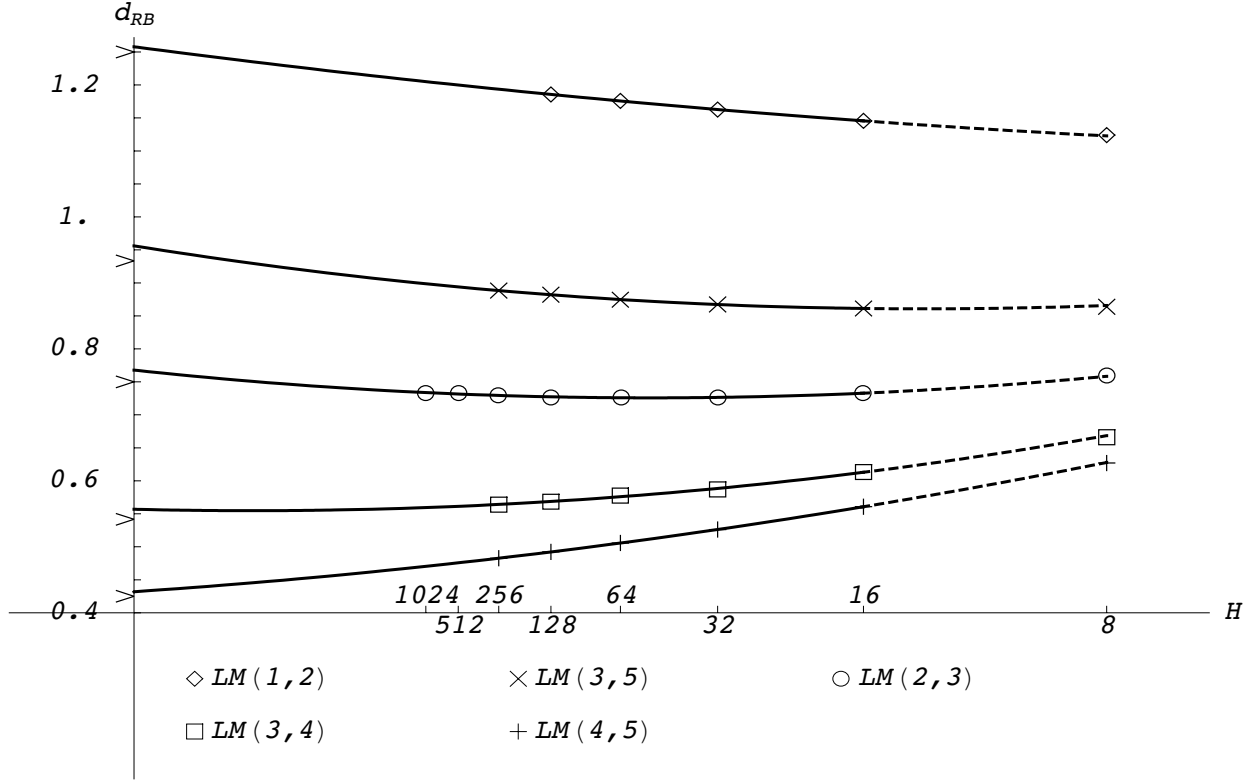


Figure 9: Measurements of d_{RB} for the five models.

lattices used	d^{theo}	8 to 64	16 to 128	32 to 256	64 to 512	128 to 1024
\widehat{d}_H	$\frac{7}{4} = 1.750$	1.7502	1.7500	1.7501	1.7502	1.7506
\widehat{d}_{EP}	$\frac{4}{3} \sim 1.333$	1.365	1.342	1.333	1.330	1.331
\widehat{d}_C	$\frac{91}{48} \sim 1.896$	1.815	1.854	1.875	1.886	1.891
\widehat{d}_{RB}	$\frac{3}{4} = 0.750$	0.6880	0.7176	0.7342	0.7428	0.7477

Table 6: Measurements \widehat{d} for the four masses of critical percolation $\mathcal{LM}(2,3)$ obtained from a subset of the data.

from top to bottom and the right one from bottom to top. Finally, EP3 adds to the quarter-circles of EP1 the “inner bubbles”, cf. the discussion above.

In our simulations, the definitions EP1 and EP2 appear to have the same thermodynamical limit and converge to the predicted value, whereas definition EP3 seems to behave in the limit as the hull itself. Even though critical dense polymers has the densest hull among the models considered, it cannot be used to explore the three definitions of EP as some of them fail for this model. Instead, we present here data for

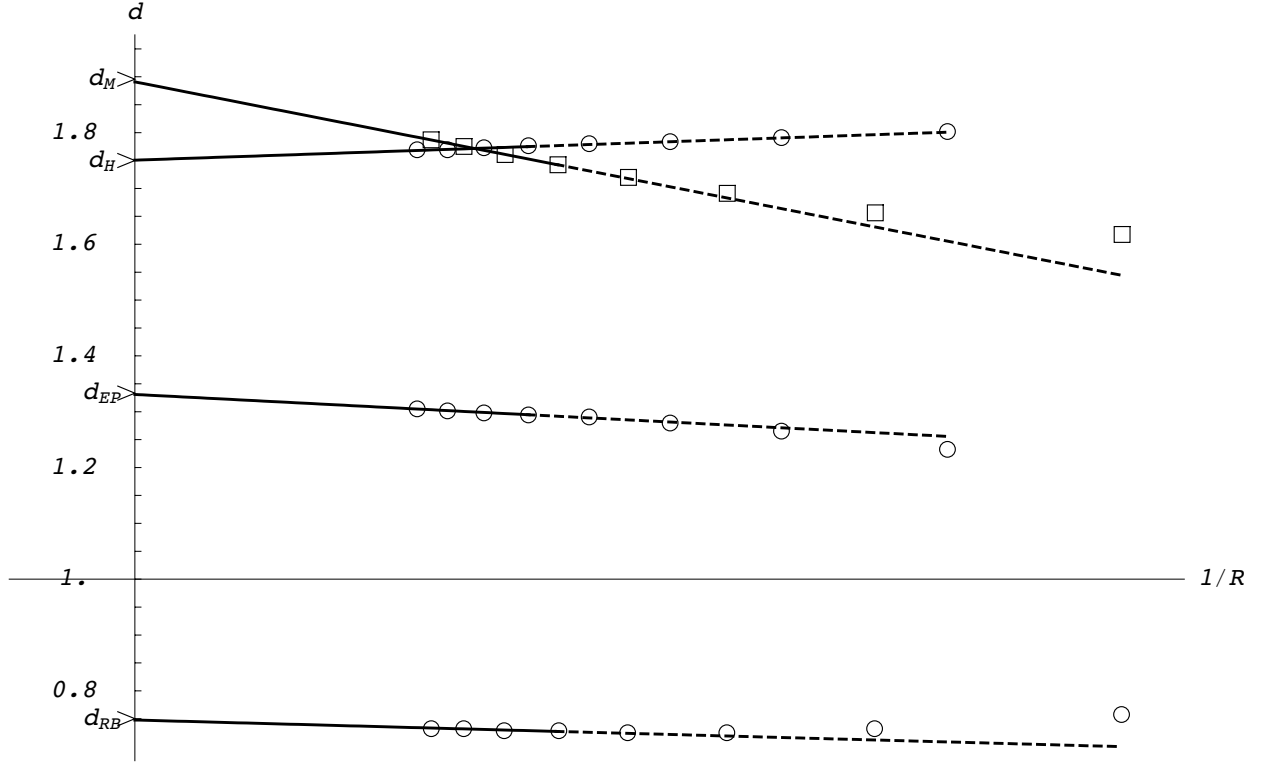


Figure 10: Masses for critical percolation $\mathcal{LM}(2, 3)$. Squares have been used exceptionnally for the cluster mass data to distinguish them from those of the hull. Fits are obtained using only the four largest lattices ($H = 128, 256, 512$ and 1024). Data for d_H and d_{EP} are compiled with a different definition of R than those of d_D and d_{RB} ; this accounts for the different horizontal alignment.

$\mathcal{LM}(3, 5)$. After critical dense polymers, it is the model with the densest hull. The other models behave similarly to $\mathcal{LM}(3, 5)$. As the densest, the hull of $\mathcal{LM}(3, 5)$ is the one most likely to feel the boundaries and the two defects may impact each other. Figure 11 shows how the three definitions behave for lattices from $H = 8$ to 256 . Fits with a quadratic term are obviously necessary, at least for EP1 and EP3; we use a quadratic term in the three fits, rejecting the smallest lattice in the three cases (and the $H = 16$ for EP2). The definition EP2 explores the side of the defects closest to the boundary and one might have thought that the hull would hit the boundary often; this would then bring its external perimeter EP2 closer to be linear, lowering its fractal dimension towards 1. This is not the case. Actually, for all lattice sizes, EP2 remains larger than EP1, simply because it adds the contribution of both defects. If the density of EP2 is somewhat decreased by the boundary, our data do not reveal this.

Obviously, the thermodynamical limit of the definition EP3 is not the predicted one with fractal dimension $\frac{13}{10}$. For $\mathcal{LM}(3, 5)$ and all other models, the extrapolation of the data we have seems to bring its limit very close to d_H . Because of the definition of EP3, $d_{EP3} \leq d_H$. As it nevertheless seems to overshoot d_H a little bit, a possible resolution is that the definition EP3 actually *converges* to the hull.³ If this guess is true, then it would mean that, as the lattice grows, the inner bubbles account for a fixed ratio of the hull. This is surprising because previous experiments did not see this. Of course, an explanation could be that the loop and spin external perimeters are physically different objects. But what about the definitions EP1 and EP2 which *do* reproduce the dimensions of the spin external perimeter? A second possible explanation is the following. The external perimeter EP3 is that of one of the largest, if not the largest, geometric objects in

³The fact that it overshoots is of no real concern considering the extreme extrapolation that had to be done! Note that the data $\hat{d}_{EP3}^{H \times V}$ are in the range $[1.25, 1.52]$ and the extrapolated value is 1.88. This is not for the faint-hearted ...

the lattice. It is conceivable that inner bubbles play a significant role only in the largest objects. But in other experiments, fits are done on objects of all sizes within the lattice. (See for example the comment at the end of Section IV A. of [13].) Could the fits of these experiments have minimized the contribution of the largest objects? Yet a third explanation could be that, in adding the inner bubbles, we give them too much weight. Indeed, by comparing Figure 5 (d) and Figure 7 (d), we see that, where there is a single “inner spin” of the spin EP, we count 12 quarter-circles in the loop EP. Resolving this question requires more simulations.

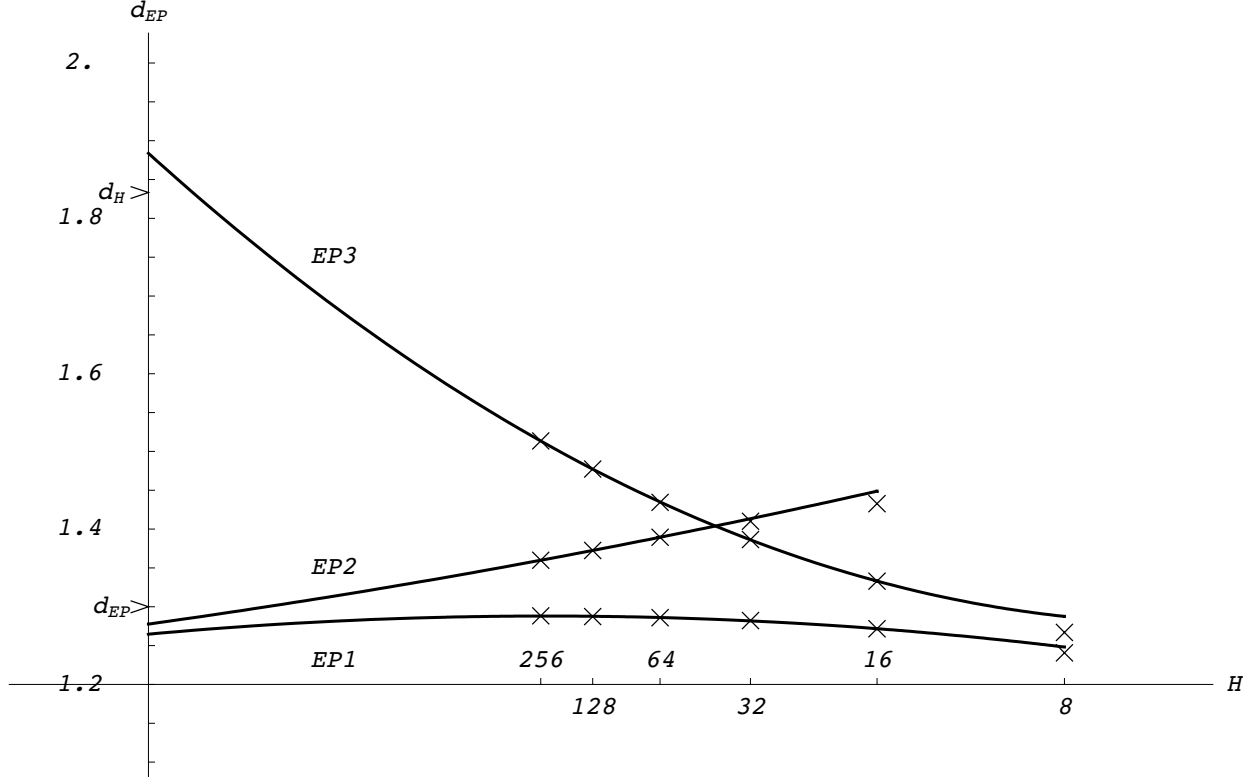


Figure 11: The three definitions of the *loop external perimeter* for the model $\mathcal{LM}(3, 5)$.

4.3.3 d_H and d_{EP} for configurations with one and two defects

We have just seen that, for the left defect, EPs drawn by a right-bias walker (EP2) or by a left-biased walker (EP1) seem to have the same thermodynamical limit. This rules out a significant effect of the boundary on that geometric object. What about the influence of the right defect on the left one? One could argue that the right defect acts, for the left defect, as boundary on its right side and therefore should have no more effect on it than the boundary. This seems to be the case.

Two sets of measurements are taken: one set on configurations with two defects (as we have done earlier) and a second one with only the left defect. The right defect is actually left in order not to change the size of the lattice, but is forced to remain along the top, right and bottom boundaries. The smallest sample is 10^5 . On these two sets of configurations, we measure d_H of the left defect and its d_{EP} with a right-biased and a left-biased rule. Figure 12 draws measurements of d_H and d_{EP} of the left defect for the model $\mathcal{LM}(3, 5)$. Measurements with two defects are represented by dashed lines. In all cases, they lie under their counterparts measured with only one defect. This is natural because, in the latter configuration, the defect has more space to wander in and it takes advantage of this. The four curves for the external perimeter are well separated over $H = 128$. The two obtained from a left-biased rule are over the other two with a right-biased one. Recall that the right-biased rule forces the external perimeter of the left defect to collide

often with the left boundary of the lattice. Consequently, the external perimeters thus obtained tend to have fewer quarter-circles than the two drawn with the left-biased rule. So the order in which the curves appear in the figure was predictable. But what is new is that the two ways of measuring d_H appear to have the *same* thermodynamical limit, and similarly for the four ways of measuring d_{EP} . This confirms our intuitive statement.

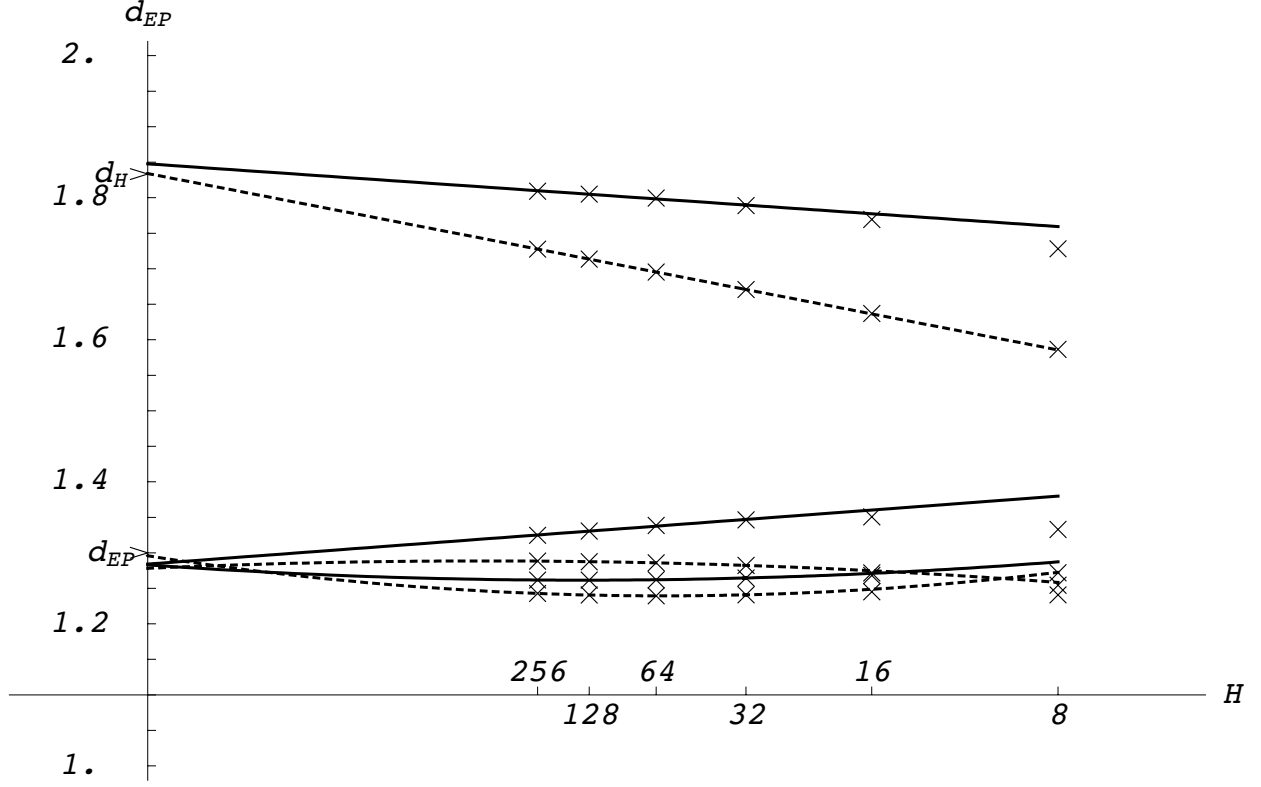


Figure 12: Measurements for the model $\mathcal{LM}(3,5)$ of d_H and d_{EP} of the left defect with and without the right defect.

Acknowledgements

This work is supported by the Australian Research Council and the Canadian Natural Sciences and Engineering Research Council.

A Loop gas and logarithmic minimal models

We recall here the definitions of the loop gas and logarithmic minimal models $\mathcal{LM}(p, p')$ on the lattice. Each elementary face or box of a finite rectangular lattice, with H horizontal boxes and V vertical ones, is restricted to be in one of the two configurations in Figure 13 with the Boltzmann weights

$$\sigma_1 = \frac{\sin(\lambda - u)}{\sin \lambda}, \quad \sigma_0 = \frac{\sin u}{\sin \lambda}. \quad (\text{A.1})$$

The crossing parameter $\lambda \in (0, \frac{\pi}{2}]$ labels the given loop model with loop fugacity

$$\beta = 2 \cos \lambda. \quad (\text{A.2})$$

The parameter u is the *spectral parameter*. For real values, it measures the spatial anisotropy of the lattice. The simulations in the present paper are all carried out at the isotropic point $u = \lambda/2$. In this case, the two box states in Figure 13 are equally probable, as $\sigma_0 = \sigma_1$.



Figure 13: The two configurations of an elementary face with weights $\sigma_1 = \frac{\sin(\lambda-u)}{\sin \lambda}$ and $\sigma_0 = \frac{\sin u}{\sin \lambda}$.

There are many ways of fixing the boundary conditions. For the present discussion, let us join all loop ends at the four boundary segments to a nearest neighbour belonging to the same boundary segment. A 4×4 configuration is shown in Figure 14. The Boltzmann weight of a configuration is determined by three

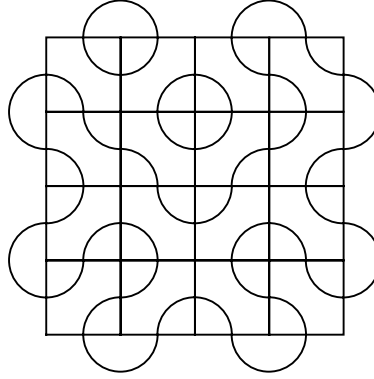


Figure 14: A configuration on a 4×4 lattice.

numbers: the number $\#_1$ of boxes in state 1, the number $\#_0 = H \times V - \#_1$ of boxes in state 0 and the number ℓ of closed loops. The statistical weight is then

$$P(\#_0, \#_1, \ell) = \sigma_1^{\#_1} \sigma_0^{\#_0} \beta^\ell / Z \quad (\text{A.3})$$

where the normalization factor (the partition function) Z assures that the sum of the $P(\#_0, \#_1, \ell)$ over all $2^{H \times V}$ configurations is 1. In the isotropic case, the lattice model depends on the single parameter, the loop fugacity β , and the probability of a configuration is determined by the number of loops that it contains. Care has to be taken if $\beta = 0$ since the partition function itself vanishes with the boundary conditions indicated in Figure 14. This does not concern us here since the boundary conditions used in the bulk part of this paper all involve at least one so-called defect.

As a CFT, the generic loop gas is described by the Coulomb gas [23]. When $\frac{\lambda}{\pi}$ is rational, however, the model has some remarkable properties. Assuming $0 < \lambda < \pi$, there then exist coprime integers p and p' such that $p' > p$ and

$$\lambda = \frac{(p' - p)\pi}{p'} = \left(1 - \frac{1}{\bar{\kappa}}\right)\pi, \quad \bar{\kappa} = \frac{p'}{p}. \quad (\text{A.4})$$

This choice of crossing parameter defines the logarithmic minimal model $\mathcal{LM}(p, p')$. It is argued in [24] that the continuum scaling limit of the loop gas with these special values of λ yields a *logarithmic* CFT [25], denoted by $\mathcal{LM}(p, p')$ and with central charge

$$c = 1 - \frac{6\lambda^2}{\pi(\pi - \lambda)} = 1 - \frac{6(p' - p)^2}{pp'}. \quad (\text{A.5})$$

Particular examples of these continuum limits correspond to critical dense polymers $\mathcal{LM}(1, 2)$, critical percolation $\mathcal{LM}(2, 3)$ and the logarithmic Ising model $\mathcal{LM}(3, 4)$. It is noted that, even though this paper reports measurements only for *rational* λ/π , the definition of a loop gas on a finite lattice holds for *every* λ .

B Upgrade algorithms

B.1 Critical percolation ($\beta = 1$)

Critical percolation is described by $\mathcal{LM}(2, 3)$ where $\lambda = \frac{\pi}{3}$ and $c = 0$. For the purpose of simulations, this is the simplest case as $\beta = 2 \cos \lambda = 1$ and all configurations are equiprobable at the isotropic point where $u = \frac{\lambda}{2} = \frac{\pi}{6}$. At this point, we sample the configuration space according to (A.3) by choosing randomly the state of each box of the $H \times V$ lattice, giving each state in Figure 13 equal probability. Since $\beta = 1$, no loop counting is required and obtaining good samples on large lattices can be done swiftly.

B.2 Models with $0 < \beta \leq 2$

For $\lambda \in [0, \frac{\pi}{2})$, the loop fugacity β ranges in $(0, 2]$. For $\beta < 1$, the probability P (A.3) can be seen as penalizing configurations with a large number of loops. On the contrary, for $\beta > 1$, configurations with many loops are favoured. For $\beta \neq 1$, an upgrade algorithm is needed to sample the space with the correct probability.

We recall that the Swendsen-Wang algorithm takes advantage of the FK representation of the Potts model. For spin models, like the Q-Potts model, the Swendsen-Wang algorithm provides an efficient way to upgrade configurations. From a given spin configuration where each site is in one of the Q available states, the Swendsen-Wang algorithm first constructs an FK configuration by removing bonds between neighbouring sites that are not in the same state and by keeping, with probability $p = p(Q)$, bonds between neighbouring sites in the same state. The FK graphs are in one-to-one correspondence with the loop gas configurations. The second step of the algorithm simply chooses one of the Q possible states for each of the connected components of the FK graph. But this is meaningful only if Q is an integer. The relationship between the number of states Q of the Potts model and the fugacity is $Q = \beta^2$. Except for $\beta = 1, \sqrt{2}, \sqrt{3}$ and 2, the corresponding Q of the loop gas will not be an integer and the second step of the Swendsen-Wang algorithm cannot be extended in an obvious fashion.

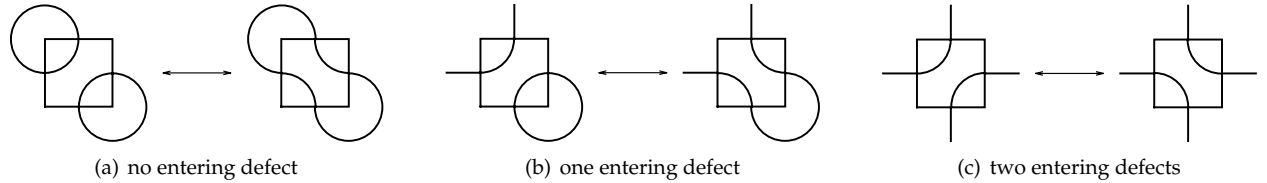


Figure 15: The effect of flipping one box on the number of loops.

We therefore use the traditional Metropolis algorithm, flipping one box or a small number of them at a time. Suppose that we have allowed defects to enter and exit the configurations. Flipping one box will always change the number of loops by 0, +1 or -1 . This is demonstrated in Figure 15. The first pair shows the situation where the two quarter-circles of the box being flipped belong to closed loops. The portion of the closed loops outside the box may contain a large number of quarter-circles. We represent them as small “ears”. The configuration before the box flip is one of the two configurations represented in Figure 15 (a) and the configuration after is necessarily the other one. The change in the number of loops is therefore ± 1 . Figure 15 (b) depicts the case where one of the two quarter-circles belong to a defect. The external parts of the defect are represented as segments. Again, the change is ± 1 loop. If two distinct defects cross the box as in Figure 15 (c), its flipping does not change the total number of loops. Note that if the same defect crosses

the box twice, the situation is that of the right drawing of Figure 15 (b) and a loop will be created by the flipping process.

The simplest MC algorithm is therefore to flip one box at a time. The box is chosen at random in the $H \times V$ lattice. If the number of loops has not changed (as in Figure 15 (c)), we accept the flip. If the number of loops has changed, the ratio

$$\frac{P(\text{configuration after flip})}{P(\text{configuration before the flip})} = \beta^{\pm 1} \quad (\text{B.1})$$

is computed. If this ratio is larger than one, the change is accepted. If it is smaller than one, the change is accepted with probability given by the ratio. If this algorithm is used repeatedly, the probability of visiting any configuration starting from any other is nonzero. This is the usual Metropolis algorithm.

In order to calculate the change in the number of loops, it suffices to construct the loops intersecting the box being flipped. All our simulations involve one or two defects and these are large. It might therefore be useful to flip several boxes at a time, as several could intersect defects. There is a compromise to be struck between changing many boxes, to speed up the upgrading, and maximizing the acceptance rate. Fortunately, the acceptance rate does not fall too quickly as the number of boxes being flipped is increased. This can be seen as follows. Let x denote one of the $H \times V$ boxes of the lattice and let σ_x be a given configuration on all boxes but x . The choice of state for the box x gives rise to two configurations for the whole lattice. If both defects cross box x , then the acceptance rate is 1 since the number of loops is unchanged. Exclude now the case of two defects crossing x . The difference between the numbers of loops between these configurations is then ± 1 . If the configuration with the largest number of loops is σ_x^+ and the other σ_x^- , the ratio of their probabilities is

$$\frac{P(\sigma_x^+)}{P(\sigma_x^-)} = \frac{P(\sigma_x^+|\sigma_x)}{P(\sigma_x^-|\sigma_x)} = \beta \quad (\text{B.2})$$

and the sum of the conditional probabilities is 1. We thus have

$$P(\sigma_x^-|\sigma_x) = \frac{1}{\beta + 1} \quad \text{and} \quad P(\sigma_x^+|\sigma_x) = \frac{\beta}{\beta + 1}. \quad (\text{B.3})$$

Suppose now that $\beta < 1$ and then $P(\sigma_x^-|\sigma_x) > P(\sigma_x^+|\sigma_x)$. If we start from σ_x^+ , the flip of x will be accepted with probability 1 and, if we start from σ_x^- , it will be accepted with probability β . The acceptance rate is therefore

$$r = P(\sigma_x^+|\sigma_x) + \beta P(\sigma_x^-|\sigma_x) = \frac{2\beta}{\beta + 1}, \quad \beta < 1. \quad (\text{B.4})$$

Likewise for $\beta > 1$, one gets

$$r = 2/(1 + \beta), \quad \beta > 1. \quad (\text{B.5})$$

The acceptance rate is therefore

$$r = 2 \min(P(\sigma_x^+|\sigma_x), P(\sigma_x^-|\sigma_x)). \quad (\text{B.6})$$

What is the acceptance rate when several boxes are flipped at once? Since a loop could cross more than one of the boxes flipped, the analysis is more delicate. But if the number n of boxes flipped is much smaller than $H \times V$, the hypothesis, that no loop crosses more than one of these n boxes, is reasonable. Let σ_- be the configuration with the smallest number of loops among the 2^n configurations under consideration. Let p_- be its conditional probability, that is, its probability given that the other $(H \times V) - n$ boxes are held fixed. If $\beta < 1$, then σ_- is the most probable and a calculation similar to the previous one leads to the acceptance rate of

$$r \sim \left(\frac{1 + (-1)^n}{2} \binom{n}{n/2} \beta^{n/2} + 2 \sum_{0 \leq i < n/2} \binom{n}{i} \beta^{n-i} \right) p_-. \quad (\text{B.7})$$

The result is the same if $\beta > 1$. In either case, the probability p_- is

$$p_- = (1 + \beta)^{-n}. \quad (\text{B.8})$$

As an example, the acceptance rate for the logarithmic Ising model ($\beta = \sqrt{2}$) of the flip of a single box is 82% and that of the flip of 20 boxes is 45%, always under the assumption that no loop crosses more than one of these 20 boxes. On large lattices ($H \times V = 128 \times 128$ or larger), the measured acceptance rate \hat{r} is the one calculated, within measurement error. The assumption on loops crossing the boxes being flipped is thus confirmed as being reasonable. By flipping several boxes at once, we save some overhead in the upgrade process and time when more than one of the n boxes intercept the defects.

In Section 4.2, we study configurations with two defects. There are two entry points at the top of the lattice and two at the bottom. Our study conditions the defects to enter from the top and exit at the bottom. The algorithm is not forcing the production of configurations with defects running vertically only. That is, the algorithm gives also configurations where the defect entering at the top left entry point exits at the top right one. We reject these and keep for measurements only those where the defect entering at the top left entry point exits at the bottom left exit point. Since upgrades are (time) expensive, we have explored the following way of gaining time. After the completion of the number of upgrades necessary for independence, we check whether the defects are vertical. If they are not, we perform upgrades (checking between each) until the new configuration has vertical defects. This unfortunately biases the MC process. Indeed, choosing the first configuration with vertical defects after a run of configurations without them is likely to shift the distribution, probably onto configurations that have a constriction point (where the two defects have switched from a left-right to top-bottom pattern). To avoid this bias, a configuration without vertical defects is simply rejected and a full number of upgrades is redone before checking for vertical defects and possible measurement.

B.3 Critical dense polymers ($\beta = 0$)

This case is particular because, for $\beta = 0$, loops of any size are forbidden. Defects are thus necessarily present and must fill the lattice. We have developed a (very slow) algorithm to generate randomly dense polymer configurations with two defects. The difficulty here is not to sample the configuration space with the correct probability. As for critical percolation, all (admissible) configurations are equiprobable. The problem is to make sure that they do not contain loops. Suppose that we are interested in configurations where two defects enter at the top edge of a rectangular lattice and exit at the bottom edge, and that a configuration without loops is already known. The entry and exit points are fixed throughout the simulations. The algorithm first lists all boxes that are crossed by both defects. This list is never empty. One of these boxes is then chosen randomly with uniform probability and flipped. The type of flip is the one depicted in Figure 15 (c) and the resulting configuration is also without loops. However, one of the defects enters from and exits at the top while the other goes bottom to bottom. By repeating the algorithm we get a new configuration with no loops and two defects crossing the lattice from top to bottom.

How does one get a starting configuration without closed loops? We fill the lattice randomly. The result is a configuration with (in general) many loops and two defects. We then repeat the following step. We list boxes that are crossed only once by either defect. If there is a closed loop, this list is non empty. We then flip one of these boxes, thereby changing the left configuration of Figure 15 (b) to its right companion, and start over. At the end we can check that the defects cross from top to bottom and, if necessary, correct by (half) the above algorithm.

C Initial thermalization and independence of measurements

Let us call an MC step the trial of flipping 20 boxes at once. We have established experimentally the number of MC steps necessary to assure that measurements of fractal dimension of defects or of other masses are statistically independent. As is well-known, this number of steps strongly depends on the model. For example, the 4-Potts model requires a significantly larger number of steps than the Ising model. For large lattices, we use the following number of MC steps between measurements

$$\frac{H \times V}{8 \times 20} d(\beta) \quad (\text{C.1})$$

where $d(\beta)$ is a factor dependent on the model: $d = 1$ for $\mathcal{LM}(3, 5)$, $d = 2$ for the logarithmic Ising model $\mathcal{LM}(3, 4)$ and $d = 4$ for the logarithmic tricritical Ising model $\mathcal{LM}(4, 5)$. Hence, for $\mathcal{LM}(3, 5)$, we try to flip one eighth of the boxes (by trials of 20 boxes) between measurements. This number goes up to one half for $\mathcal{LM}(4, 5)$. A finer analysis is under way and will be published elsewhere. It confirms that these numbers are fine, probably on the zealous side.

The initial random configuration is thermalized by 1000 times the number of MC steps just listed. The initial thermalization is therefore four times longer for $\mathcal{LM}(4, 5)$ than for $\mathcal{M}(3, 5)$. Again, we think that this is satisfactory, if not “too prudent”, but this is harder to assess. We have experimented with the (spin) Ising model and compared it with the $\beta = \sqrt{2}$ loop gas as follows. First, we use an ordinary Ising spin lattice wrapped on a cylinder at the critical temperature. There are four times as many spins along the cylinder than along the circular sections. We measure the two-point spin correlation function on the section in the middle of the cylinder using many samples of 10^3 configurations (chosen to be independent). We then perform the same experiment with the corresponding loop gas. We know that a loop configuration can be interpreted as an FK configuration and therefore that a spin configuration can be constructed from it. We repeat several times the following experiment: from a random configuration, we apply N MC steps and then proceed to measure the spin correlation function with 10^3 configurations, each separated by the number of MC steps assuring statistical independence. By comparing the distributions of the correlation function for the spin model, on one hand, and the loop gas on the other hand, we find that it is sufficient to use the N stated earlier, that is $N = 1000$, times the number of MC steps between measurements.

For critical dense polymers ($\beta = 0$), no initial thermalization is necessary. We flip $H \times V/8$ boxes between measurements.

As the boxes are chosen randomly (for critical dense polymers and the other models), the number of boxes actually flipped might be smaller since, for example, the same box can be flipped twice between two measurements. Moreover, if a box is chosen more than once among the 20 being flipped, it will be flipped only once and the total number of boxes flipped during this Metropolis step will be smaller than 20. This assures that the number of boxes flipped at each step can be of either parity.

We use L'Écuyer and Tezuka's pseudo-random number generator [35] in the simulations.

References

- [1] L. Onsager, *Crystal statistics I: A two-dimensional model with an order-disorder transition*, Phys. Rev. **65** (1944) 117–149.
- [2] R.J. Baxter, *Exactly solved models in statistical mechanics*, Academic Press (1982).
- [3] P. Di Francesco, P. Mathieu, D. Sénéchal, *Conformal field theory*, Springer (1996).
- [4] O. Schramm, *Scaling limits of loop-erased random walks and uniform spanning trees*, Israel J. Math. **118** (2000) 221–288, arXiv:math/9904022.
- [5] G.F. Lawler, *An introduction to the stochastic Loewner evolution*, Proceedings of conference on random walks at Erwin Schrödinger Institute, Vienna (2001).
- [6] W. Werner, *Random planar curves and Schramm-Loewner evolutions*, Springer Lecture Notes Math. **1840** (2004) 107–195, arXiv:math/0303354.
- [7] J. Cardy, *SLE for theoretical physicists*, Annals Phys. **318** (2005) 81–118, arXiv:cond-mat/0503313v2.
- [8] W. Kager, B. Nienhuis, *A guide to stochastic Loewner evolution and its applications*, J. Stat. Phys. **115** (2004) 1149–1229, arXiv:math-ph/0312056.
- [9] M. Bauer, D. Bernard, *2D growth processes: SLE and Loewner chains*, Phys. Rept. **432** (2006) 115–221, arXiv:math-ph/0602049.

- [10] B. Duplantier, *Conformal random geometry*, Les Houches, Session LXXXIII, 2005, Mathematical Statistical Physics, A. Bovier, F. Dunlop, F. den Hollander, A. van Enter and J. Dalibard, eds., pp. 101–217, Elsevier B. V. (2006), arXiv:math-ph/0608053.
- [11] V. Beffara, *Hausdorff dimensions for SLE₆*, *Annals of Probability* **32** (2004) 2606–2629, arXiv:math/0204208; *The dimension of the SLE curves*, arXiv:math/0211322.
- [12] H. Saleur, *Conformal invariance for polymers and percolation*, *J. Phys.* **A20** (1987) 455–470; H. Saleur, B. Duplantier, *Exact determination of the percolation hull exponent in two dimensions*, *Phys. Rev. Lett.* **58** (1987) 2325–2328; B. Duplantier, H. Saleur, *Exact fractal dimension of 2D Ising clusters*, *Phys. Rev. Lett.* **63** (1989) 2536–2536; D. Ridout, *On the percolation BCFT and the crossing probability of Watts*, arXiv:0808.3530 [hep-th].
- [13] J. Asikainen, A. Aharony, B.B. Mandelbrot, E.M. Rauch, J.-P. Hovi, *Fractal geometry of critical Potts clusters*, *Euro. Phys. J.* **B34** (2003) 479–487, arXiv:cond-mat/0212216.
- [14] W. Janke, A.M.J. Schakel, *Fractal structure of spin clusters and domain walls in the two-dimensional Ising model*, *Phys. Rev.* **E71** (2005) 036703, arXiv:cond-mat/0410364.
- [15] W. Janke, A.M.J. Schakel, *Two-dimensional critical Potts and its tricritical shadow*, *Brazilian Journal of Physics* **36** (2006) 708–716, arXiv:cond-mat/0612650.
- [16] J.W. Essam, *Graph theory and statistical physics*, *Disc. Math.* **1** (1971) 83–112; C.M. Fortuin, P.W. Kasteleyn, *On the random cluster model. I. Introduction and relation to other models*, *Physica* **57** (1972) 536–564.
- [17] R.B. Potts, *Some generalized order-disorder transformations*, *Proc. Camb. Phil. Soc.* **48** (1952) 106–109; F.Y. Wu, *The Potts model*, *Reviews of Modern Physics* **54** (1982) 235–268.
- [18] R.H. Swendsen, J.-H. Wang, *Non-universal critical dynamics in Monte Carlo simulation*, *Phys. Rev. Lett.* **58** (1987) 86–88.
- [19] A.A. Belavin, A.M. Polyakov, A.B. Zamolodchikov, *Infinite conformal symmetry in two-dimensional quantum field theory*, *Nucl. Phys.* **B241** (1984) 333–380.
- [20] G.E. Andrews, R.J. Baxter, P.J. Forrester, *Eight-vertex SOS model and generalized Rogers-Ramanujan identities*, *J. Stat. Phys.* **35** (1984) 193–266; P.J. Forrester, R.J. Baxter, *Further exact solutions of the eight-vertex SOS model and generalizations of the Rogers-Ramanujan identities*, *J. Stat. Phys.* **38** (1985) 435–472.
- [21] C. Ding, X. Qian, Y. Deng, W. Guo, H.W.J. Blöte, *Geometric properties of two-dimensional O(n) loop configurations*, arXiv:cond-mat/0608547.
- [22] J.L. Cardy, *ADE and SLE*, *J. Phys.* **A40** (2007) 1427–1438, arXiv:math-ph/0610030.
- [23] B. Nienhuis, *Coulomb gas formulation of two-dimensional phase transitions*, in *Phase Transitions and Critical Phenomena*, Vol. 11, eds. C. Domb and J.L. Lebowitz (1987); P. Di Francesco, H. Saleur, J.-B. Zuber, *Relations between the Coulomb gas picture and conformal invariance of two-dimensional critical models*, *J. Stat. Phys.* **49** (1987) 57–79; *Generalized Coulomb-gas formalism for two dimensional critical models based on SU(2) coset construction*, *Nucl. Phys.* **B300** (1988) 393–432.
- [24] P.A. Pearce, J. Rasmussen, J.-B. Zuber, *Logarithmic minimal models*, *J. Stat. Mech.* **0611** (2006) P017, arXiv:hep-th/0607232.
- [25] V. Gurarie, *Logarithmic operators in conformal field theory*, *Nucl. Phys.* **B410** (1993) 535–549, arXiv:hep-th/9303160; M. Flohr, *Bits and pieces in logarithmic conformal field theory*, *Int. J. Mod. Phys.* **A18** (2003) 4497–4592, arXiv:hep-th/0111228; M.R. Gaberdiel, *An algebraic approach to logarithmic conformal field theory*, *Int. J. Mod. Phys.* **A18** (2003) 4593–4638, arXiv:hep-th/0111260.
- [26] P. Mathieu, D. Ridout, *From percolation to logarithmic conformal field theory*, *Phys. Lett.* **B657** (2007) 120–129, arXiv:0708.0802 [hep-th].

- [27] S. Smirnov, *Critical percolation in the plane: conformal invariance and Cardy's formula, scaling limits*, C. R. Acad. Sci. Paris Sr. I Math. **333** (2001) 239–244.
- [28] W. Janke, M. Weigel, *Geometrical and stochastic clusters of gravitating Potts models*, Phys. Lett. **B639** (2006) 373–377, arXiv:cond-mat/0604411.
- [29] S. Fortunato, *Site percolation and phase transitions in two dimensions*, Phys. Rev. **B66** 054107 (2002) 1–5, arXiv:cond-mat/0204366.
- [30] A. Aharony, J. Asikainen, *Fractal dimensions and corrections to scaling for critical Potts clusters*, arXiv:cond-mat/0206367.
- [31] W.H. Press, S.A. Teukolsky, W.T. Vetterling, B.P. Flannery, *Numerical recipes in C*, Cambridge University Press (1992).
- [32] P.A. Pearce, J. Rasmussen, *Solvable critical dense polymers*, J. Stat. Mech. 0702 (2007) P015, arXiv:hep-th/0610273.
- [33] H.E. Stanley, *Cluster shapes at the percolation threshold: an effective cluster dimensionality and its connection with critical-point exponents*, J. Phys. **A10** (1977) L211–L220.
- [34] T. Grossman, A. Aharony, *Structure and perimeters of percolation clusters*, J.Phys. **A19** (1986) L745–L751.
- [35] S. Tezuka, P. L'Ecuyer, *Efficient and portable combined Tausworthe random number generators*, ACM Trans. on Modeling and Computer Simulation **1** (1991) 99–112.